JGR Space Physics

RESEARCH ARTICLE
10.1029/2024JA033392

Controlling Factors of the Local Time Extent of Magnetopause Reconnection: A Statistical Study

Krishna Khanal[1], Ying Zou[2], Xueling Shi[3,4], Gary Zank[1], J. Michael Ruohoniemi[3], and Kathryn McWilliams[5]

[1]Department of Space Science, University of Alabama in Huntsville, Huntsville, AL, USA, [2]Center for Geospace Storms, John Hopkins University Applied Physics Laboratory, Laurel, MD, USA, [3]Department of Electrical and Computer Engineering, Virginia Tech, Blacksburg, VA, USA, [4]High Altitude Observatory, National Center for Atmospheric Research, Boulder, CO, USA, [5]Institute of Space and Atmospheric Studies, University of Saskatchewan, Saskatoon, SK, Canada

Key Points:

- Statistical study of the extent of dayside magnetopause reconnection based on 39 space-ground conjugate observations is presented
- Wide distribution of local time extent of reconnection is observed from ~1.5 hr MLT to ~6.5 hr MLT
- Results show that solar wind speed is an important controlling factor

Supporting Information:

Supporting Information may be found in the online version of this article.

Correspondence to:

K. Khanal,
krishna.khanal@uah.edu

Citation:

Khanal, K., Zou, Y., Shi, X., Zank, G., Ruohoniemi, J. M., & McWilliams, K. (2025). Controlling factors of the local time extent of magnetopause reconnection: A statistical study. *Journal of Geophysical Research: Space Physics*, *130*, e2024JA033392. https://doi.org/10.1029/2024JA033392

Received 1 OCT 2024
Accepted 21 FEB 2025

Abstract Magnetopause reconnection is the dominant mechanism for transporting solar wind energy and momentum into the magnetosphere-ionosphere system. Magnetopause reconnection can occur along X-lines of variable extent in the direction perpendicular to the reconnection plane. Identifying the spatial extent of X-lines using satellite observations has critical limitations. However, we can infer the azimuthal extent of the X-lines by probing the ionospheric signature of reconnection, the antisunward flow channels across the ionospheric Open-Closed Field Line Boundary (OCB). We study 39 dayside magnetopause reconnection events using conjugate in situ and ionospheric observations to investigate the variability and controlling factors of the spatial extent of reconnection. We use spacecraft data from Time History of Events and Macroscale Interactions during Substorms (THEMIS) to identify in situ reconnection events. The width of the antisunward flow channels across the OCB is measured using the concurrent measurements from Super Dual Auroral Radar Network (SuperDARN). Also, the X-line lengths are estimated by tracing the magnetic field lines from the ionospheric flow boundaries to the magnetopause. The solar wind driving conditions upstream of the bow shock are studied using solar wind monitors located at the L1 point. Results show that the magnetopause reconnection X-lines can extend from a few Earth Radii (RE) to at least ~22 RE in the GSM-Y direction. Furthermore, the magnetopause reconnection tends to be spatially limited during high solar wind speed conditions.

Plain Language Summary When the solar wind magnetic field has a southward orientation, magnetic reconnection occurs near the subsolar magnetopause with variable spatial extent in the direction perpendicular to the reconnection plane. The reconnection allows the transport of solar wind mass/energy into the magnetosphere, leading to several near-earth space weather phenomena. The amount of mass/energy thus transported is affected by the spatial extent of reconnection. Despite its significance, it is not fully understood what controls the spatial extent. A major observational limitation is that sparse satellite observations of the magnetopause cannot provide information about the spatial extent. Magnetopause reconnection drives antisunward motion of plasma on the dayside ionosphere. Using observations from ground-based high-frequency radars, we can estimate the width of such flow channels and infer the spatial extent of magnetopause reconnection. We study 39 magnetopause reconnection events with simultaneous in situ and ionospheric observations. We analyze solar wind driving conditions and local magnetopause conditions concerning the measured reconnection spans. While we observe reconnection X-lines extending from a few RE to as much as 22 RE in the GSM-Y direction, data shows that solar wind velocity upstream of the bow shock is a potential controlling factor.

1. Introduction

Magnetic reconnection at the dayside magnetosphere, also called magnetopause reconnection, is the primary mechanism for transporting mass, momentum, and energy into the magnetosphere-ionosphere system. Magnetopause reconnection has temporal and spatial variabilities that modulate the mass/energy transport across the magnetopause boundary. Both temporally continuous and intermittent magnetopause reconnection events are reported. Continuous reconnection is characterized by the persistence of Alfvénic outflows, also called "jets," at the magnetopause for several hours (Frey et al., 2003; Hasegawa et al., 2016; T. Phan et al., 2004), whereas, intermittent reconnection often manifests as Flux Transfer Event (FTE) producing repetitive reconnected flux

tubes (Russell & Elphic, 1978, 1979). Continuous reconnection events also may exhibit notable variations in the reconnection rate and occur unsteadily (T. Phan et al., 2004; Rosenqvist et al., 2008; Zou et al., 2022). In the spatial sense, on the other hand, the reconnection outflows (jets) originating from the X-line have a finite azimuthal extent along the magnetopause surface in the direction perpendicular to the reconnection plane, which is referred to as the local time extent of magnetopause reconnection. This corresponds to the length of the X-line in 2-D reconnection which has an invariant "out-of-plane" direction. Including plasma and magnetic field variability in the third dimension, X-lines assume more complex structures commonly called magnetic separators.

For in situ observations, the local time extent of the magnetopause reconnection can be inferred from detection of the diffusion region or reconnection outflows at different Magnetic Local Times (MLTs) along the magnetopause boundary. This requires either simultaneous crossings of the magnetopause by multiple satellites or multiple crossings by a single satellite orbiting along the magnetopause boundary. Both are rare occurrences. Moreover, even with multipoint observations, one can not ascertain whether the reconnection is active between and away from the observation points. Studies probing the azimuthal extent of ionospheric signatures of reconnection, such as Poleward Moving Auroral Forms (PMAFs), cusp precipitation, and fast antisunward flow channels, have demonstrated that remote sensing can greatly complement the understanding of the spatial nature and extent of magnetopause reconnection (Fuselier et al., 2002; S. E. Milan et al., 2016; Pinnock et al., 2003; Zou et al., 2019). Combinations of low-orbiting satellites, auroral imagers, and radars make it possible to see the ionospheric counterparts of reconnection structures in their entirety.

Early studies based on fortuitous multiple spacecraft observation of the magnetopause revealed that reconnection during southward IMF may extend from dawn to dusk amounting to as much as a 40 RE long X-line (T. Phan et al., 2000, 2006). Those studies assumed dawn-dusk symmetry and coherency of the X-line between the observation locations. Using near-simultaneous observations of the magnetopause by 10 different satellites, Dunlop et al. (2011) presented evidence of a highly extended magnetopause reconnection line extending to dawn-dusk flank locations. Notably, the existence of widely distributed multiple reconnection sites (patches) along the extended configuration of the X-line was suggested. Some studies, based on the ionospheric signatures, have also reported evidence to support the notion of highly extended reconnection. For example, Pinnock et al. (2003) presented evidence of a 38 RE long X-line based on the azimuthal extent of antisunward plasma flow in the high latitude ionosphere. Similarly, based on the wide local time extent of reconnection-driven cusp auroral precipitation, Fuselier et al. (2002) showed that reconnection can coherently occur over a large portion of the dayside magnetopause.

Considerable evidence also supports the notion that reconnection could be spatially patchy and discontinuous. For example, "elbow type" FTEs are regarded as narrow flux tube structures emanating from an azimuthally narrow reconnection site (Russell & Elphic, 1978, 1979). In situ observation reveal that FTE-related bipolar variations are typically observed to cover a few RE along the magnetopause surface (R. Fear et al., 2008; Wang et al., 2007). Studies based on auroral signatures of FTEs show that they have variable azimuthal extents ranging from a few hundred km to over 7 hr MLT (Lockwood et al., 1990; S. Milan et al., 2000; S. E. Milan et al., 2016; Oksavik et al., 2004). Recent multipoint observations of the magnetopause have revealed that the reconnection X-line can be constrained over a limited region along the magnetopause (Atz et al., 2022; Walsh et al., 2017). Using simultaneous space-ground observations of reconnection Zou et al. (2019) showed that a the reconnection X-line can be spatially variable from patchy (a few RE) to extended (>10 RE). Studies also suggest that reconnection might start as patchy and later develop into extended reconnection with the X-line spreading in the azimuthal direction with variable speed (Jain et al., 2013; Shay et al., 2003; Shepherd & Cassak, 2012). Reconnection time ionospheric dynamics such as the motion of bifurcating auroral oval (S. Milan et al., 2000) and evolution of antisunward flow channels (Zou et al., 2018) have revealed the spreading of the reconnection X-line along the magnetopause.

While the magnetopause X-line exhibits the above variability, it is not clearly understood what controls its spatial extent. Theory and models suggest that for IMF orientations with a southward component, reconnection X-lines (anti-parallel and/or component) can exist over the entire dayside magnetopause (Cowley & Owen, 1989; Crooker, 1979; Gonzalez & Mozer, 1974; Luhmann et al., 1984; B. U. Sonnerup, 1970; Trattner et al., 2007). Nevertheless, evidence of patchy reconnection suggests that certain conditions limit the span of magnetopause reconnection. S. E. Milan et al. (2016), in a case study of two FTE events, showed that high solar wind speed might favor an azimuthally extended FTE. On the other hand, Zou et al. (2019) suggested that IMF orientation and

steadiness could be more important factors. Limited by the number of events, no conclusive results were presented.

The occurrence of high-speed jets near the magnetosphere/magnetosheath boundary is believed to be hindered by a high magnetosheath plasma beta (Paschmann et al., 1986; Scurry et al., 1994). The diamagnetic suppression condition, also called the $d\beta - \theta$ model (Swisdak et al., 2003, 2010), suggests that the flankward spreading of a reconnection X-line may be suppressed by a high plasma beta difference ($d\beta$) on either side of the magnetopause. Providing observational support to the $d\beta - \theta$ model, studies have shown that magnetopause reconnection is suppressed in the regions of low θ and high $d\beta$ along the magnetopause surface (Atz et al., 2022; T. Phan, Paschmann, et al., 2013; T. Phan, Shay, et al., 2013; Trenchi et al., 2015). Similarly, theoretical studies predict that the reconnection rate is significantly reduced as velocity shear across the magnetopause boundary exceeds the outflow speed (Borovsky, 2013; Mitchell & Kan, 1978). Generally, velocity shear and the plasma beta difference across the boundary increase away from the magnetopause nose. However, it is not clear what controls how far the X-lines can spread before those cut-off criteria are met. Similarly, theory and modeling predict that the magnetospheric mass density can play a significant role in reducing the magnetopause reconnection rate (Birn et al., 2008; Cassak & Shay, 2007). Consistent with this prediction, it is shown that the presence of cold magnetospheric plasma at the magnetopause boundary can significantly suppress the local reconnection rate (Borovsky et al., 2008, 2013; Walsh et al., 2014; Zou et al., 2021). A higher mass density may also lower the velocity shear threshold for reconnection cut-off limiting the span of the X-line (Borovsky et al., 2013).

The observational limitations of spacecraft are major factors that limit our understanding of how solar wind and local boundary conditions control the spatial extent of magnetopause reconnection. It has been demonstrated that the flow width of the antisunward flow channels on the dayside ionosphere can be used to reliably infer the length of X-lines (Chisham et al., 2008; R. C. Fear et al., 2017; S. E. Milan et al., 2016; Pinnock et al., 2003; Zou et al., 2018, 2019). However, constrained by the lack of events, few observational findings have been presented to address what controls the spatial extent of the reconnection X-line. In this work, we utilize the capabilities of space-ground conjugation to study 39 magnetopause reconnection events using THEMIS and SuperDARN observations. A pilot study based on SuperDARN-THEMIS conjugation was recently presented by Zou et al. (2019). As our first approach, we make a few important improvements in the methodology for greater objectivity. Second, we analyze solar wind driving conditions and local magnetopause conditions concerning the local time extent of the magnetopause reconnection. Solar wind data is obtained from two upstream satellite monitors, ACE and Wind. Results are compared with existing theoretical predictions.

2. Data

THEMIS (Angelopoulos, 2009b) is used for the magnetopause observation. THEMIS is a five-satellite constellation mission launched in 2007 to study the near-Earth plasma environment including the solar wind, the magnetosheath, and the magnetosphere. In 2011, THEMIS B and C were moved to the lunar orbit as a part of a separate mission. We use data from THEMIS A, D, and E to identify in situ reconnection and to study local magnetopause conditions. In the dayside science phase, the apogee of THEMIS orbits are on the dayside of the magnetosphere observing magnetopause at least twice a day. All THEMIS probes are similarly equipped. Magnetic field data is obtained from Fluxgate Magnetometer (FGM) (Auster et al., 2008). Plasma moments are obtained from the Electrostatic Analyzer (ESA) (McFadden, Carlson, Larson, Ludlam, et al., 2008) which measures ion in the energy range ~8 eV to 25 keV. Spacecraft potential data from Electric Field Instruments (EFI) (Bonnell et al., 2009) is used to derive the plasma density below the lower energy threshold of ESA. Solar wind driving conditions during the reconnection events are studied using data sets from the solar wind monitors Advanced Composition Explorer (ACE) and WIND. We use high-resolution data shifted to the bowshock nose.

Ionospheric observations are obtained from SuperDARN which is an international network of low-power high-frequency (8–20 MHz) coherent radars that observe the dynamics of Earth's ionosphere (Chisham et al., 2007; Greenwald et al., 1995; Nishitani et al., 2019). Each radar consists of 16 azimuthally organized beams forming a fan-like shape. Each beam consists of at least 75 range gates with a gate length of 45 km. In normal operation mode, the radar completes one scan in 1 or 2 min. The backscattered echoes from ionospheric irregularities are processed to obtain complex multi-lag Auto Correlation Functions (ACF) for each range gate. The ACFs are fitted using standard functions to derive the Line of Sight (LOS) velocity, spectral width, and backscatter power. The measured LOS velocity refers to the projection of F-region **ExB** drift velocity driven by the convection electric

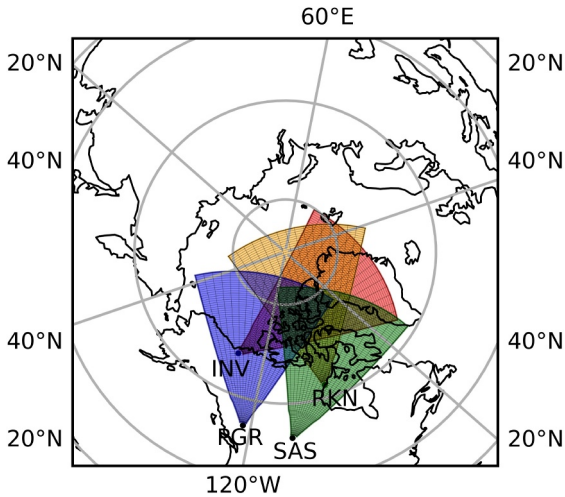

Figure 1. FOV plots for the four SuperDARN radars RKN, INV, SAS, and PGR at 19:15 UT in the geographic coordinate system. Magnetic noon lies at the lower center.

field on the beam direction (Ruohoniemi et al., 1987). Different techniques have been used to combine the available LOS velocity measurements from radars to obtain a two-dimensional velocity field (Amm et al., 2010; Bristow et al., 2016; Ruohoniemi & Baker, 1998). To analyze large-scale flow structures on the ionosphere, we use 2D velocity field data obtained from the spherical harmonic fit (SHF) method (Ruohoniemi & Baker, 1998). This method provides the "E cross B" drift velocity $\left(\mathbf{E} \times \mathbf{B}/B^2\right)$ of ionospheric charged particles over the entire F region polar ionosphere. In SHF method, the measured LOS velocities from all radars and the model data are fitted to an expansion of electrostatic potential in terms of spherical harmonic functions. Our data set uses the statistical model TS18 (Thomas & Shepherd, 2018) and the fitting parameters: order = 8 and degree = 7, to obtain a set of real-valued coefficients (A_{lm}, B_{lm}). The coefficients resulting from the fitting can be used to obtain a fitted vector at any point. However, fitted vectors derived at the locations with the radar measurements are deemed more reliable. The spectral width of the Doppler spectrum is used to identify the Open-Closed field line Boundary (OCB) location at the dayside ionosphere. We use data from the four high latitude radars, namely, Rankin Inlet (RKN; GEOLAT = 62.82°, GEOLON = −92.113°), Inuvik (INV; GEOLAT = 68.414°, GEOLON = −133.772°), Saskatoon (SAS; GEOLAT = 52.16°, GEOLON = −106.53°), and Prince George (PGR; GEOLAT = 53.98°, GEOLON = −122.59°), where GEOLAT and GEOLON stand for geographic latitude and longitude, respectively. The Field of View (FOV) of each of the four radars is shown in Figure 1. In the UT range between 15:30 and 22:30, the combination of these radars can provide good coverage of the entire dayside ionosphere, capturing the reconnection-related convection signature.

3. Methodology

3.1. In Situ Identification of Reconnection

We identify a magnetopause reconnection event based on the detection of reconnection outflow (jets) by a THEMIS satellite at the magnetopause boundary. Magnetopause crossings are identified by a transition in ion energy characteristics. For southward IMF conditions, the magnetic field component B_z also reverses at the magnetopause boundary. We use the LMN boundary normal coordinate system (Russell & Elphic, 1979) to present magnetic field and velocity measurements. In this coordinate system, N is along the magnetopause normal direction, L is along the reconnection outflow direction, and M is along the X-line. The magnetopause normal direction is obtained from the Minimum Variance Analysis Method (B. Ö. Sonnerup & Cahill, 1967; B. U. Sonnerup & Scheible, 1998).

At the dayside magnetopause, rotation in B_L accompanied by enhanced V_L is a typical indication of reconnection. We confirm reconnection by comparing the observed magnitude and direction of the jets with theoretical predictions by the Walen relation. This is based on the tangential momentum balance across a rotational discontinuity (Hudson, 1970; Paschmann et al., 1979, 1986). Following Paschmann et al. (1986), the predicted reconnection jet velocity can be written as

$$\Delta \mathbf{V}_{predicted} = \pm\left(\frac{1-\alpha_1}{\mu_0 \rho_1}\right)^{1/2}\left[\mathbf{B_2}\frac{1-\alpha_2}{1-\alpha_1} - \mathbf{B_1}\right] \quad (1)$$

where the subscripts "1" and "2" refer to the magnetosheath reference location and the magnetopause, respectively. The magnetopause location is taken at the position where maximum velocity change is observed, whereas, the magnetosheath reference interval is ∼10-s interval taken at the magnetosheath just outside the magnetopause. The magnetosheath mass density is determined by assuming plasma composed of 95% proton and 5% helium. The anisotropy factor α is defined as

$$\alpha = \left(p_{\parallel} - p_{\perp}\right)\mu_0/B^2. \quad (2)$$

Agreement between the theoretical prediction and observation can be evaluated by a dimensionless quantity

$$\Delta V^* = \frac{\Delta \mathbf{V}_{predicted} \cdot \Delta \mathbf{V}_{observed}}{\Delta V_{predicted}^2} \quad (3)$$

where $\Delta \mathbf{V}_{observed}$ is the ion velocity change compared to background velocity at magnetosheath reference location. $\Delta V^* > 0.5$ indicates a good agreement (Atz et al., 2022; Paschmann et al., 1986; Zou et al., 2019).

It is to be noted that the Walen test may not predict the outflow speed earthward from the point where magnetospheric density falls below 20% of the magnetosheath density due to the effects of the slow mode expansion fan (T. D. Phan & Paschmann, 1996). We compute the predicted velocity at each data point within the interval between the magnetosheath reference location and the point where the magnetospheric density starts falling below 20% of the magnetosheath density. A reasonable match between the predicted and the observed speed profile is expected for the reconnection events.

3.2. Remote Sensing

For southward IMF conditions, reconnection occurs at the subsolar magnetopause. This creates highly curved open field lines over a certain azimuthal extent along the magnetopause surface. The open field lines convect antisunward over the polar caps on both hemispheres and subsequently undergo tail reconnection. The tail reconnection creates closed field lines that return toward the dayside along the flank regions forming a cyclic convection of magnetic field lines called the "Dungey Cycle" (Dungey, 1961). On the field line footprints in the high latitude ionosphere, plasma is driven in a similar cyclic motion forming a characteristic two-cell convection pattern. Thus, the width of the antisunward flow region on the dayside ionosphere across the OCB serves as an ionospheric measure of the azimuthal extent of the magnetopause reconnection (also called the "merging gap") (Chisham et al., 2008; Cowley & Lockwood, 1992).

We identify the OCB using the two well-established ionospheric proxies: the Spectral Width Boundary (SWB) and the Convection Reversal Boundary (CRB). In SuperDARN measurements, SWB is defined as a location where the Doppler spectral width abruptly changes from low to high values. Higher SWB is found to be associated with cusp particle precipitation (Baker et al., 1995; Moen et al., 2001). It is demonstrated to be a reliable proxy of OCB on the dayside ionosphere (Chisham & Freeman, 2004; Chisham, Freeman, Lam, et al., 2005). Several threshold techniques have been applied to spectral width data to identify the SWB (Baker et al., 1997; Chisham & Freeman, 2003; Chisham et al., 2001; Pinnock et al., 1999). These methods require a threshold value specification for the spectral width whose optimum choice depends on the individual spectral width distribution and magnetic local time (Chisham & Freeman, 2004). A range of spectral width values from 150 to over 300 m/s have been routinely used to identify the SWB (Chisham & Freeman, 2004; Chisham, Freeman, Lam, et al., 2005; Chisham, Freeman, Sotirelis, & Greenwald, 2005). Although the choice of the threshold is arbitrary, the identified locations do not differ significantly if the jump in the spectral width is abrupt and the threshold falls somewhere midway between the mean distribution on either side of the boundary. It is demonstrated that, on the dayside ionosphere near the cusp region, SWBs typically have sharp transitions (Chisham & Freeman, 2004). Statistically, 150 m/s is found to be an effective boundary threshold (Baker et al., 1997; Chisham & Freeman, 2003; Zou et al., 2021). We primarily use the threshold of 150 m/s for SWB identification. Nevertheless, we also assess the effect of using higher thresholds in our analysis.

Our threshold method is adopted from Chisham and Freeman (2003) which involves spatio-temporal median filtering of spectral width data for reliable identification of SWB. We impose a few additional rules to handle cases where a data gap exists at the range gates equatorward from the identified SWB location. It has been shown that SWB identified in near meridional beams is a more reliable proxy for OCB in the 10–14 MLT sector (Chisham, Freeman, Sotirelis, & Greenwald, 2005). Following the suggestion of Chisham, Freeman, Sotirelis, and Greenwald (2005), we select four beams on either side of the meridional beams to perform the CF-threshold method. The following steps are employed:

1. Measurements flagged as the ground scatter refer to non-ionospheric echoes and are excluded. They typically have small (<30 m/s) LOS velocity and spectral width. Similarly, backscatter with power less than 3 dB are excluded;

2. Spatial median filtering across three consecutive beams;
3. Temporal median filtering across five consecutive scans;
4. Starting at the first spectral width value along each beam, a poleward search is done until the defined threshold is exceeded. The transition is accepted as an SWB if the following criteria are met:
   (a) There are at least two non-zero spectral width measurements below the candidate location.
   (b) The median of three spectral width values poleward from the candidate location is also greater than the threshold. This criterion introduces additional spatial median filtering along the beam direction.

The transition must be identified after the tenth range gate. The range gates closer to the radar locations likely correspond to E-region scattering (Chisham & Pinnock, 2002; Forsythe & Makarevich, 2017; Thomas & Shepherd, 2018). Therefore, any transition identified below the tenth range gate is discarded. Furthermore, data over 2,000 km (roughly corresponding to the 41st range gate) away from the radar location may be problematic owing to geolocation uncertainties in the range finding algorithm (Chisham et al., 2008). Therefore, any transition identified beyond the 41st range gate is also discarded.

CRB, the second proxy of OCB that we use, is defined as the location where ionospheric convection changes from sunward to antisunward. Sunward and antisunward flows are typical of closed and open field lines, respectively. Considerable evidence shows that CRBs are well correlated with OCBs (Lockwood, 1997; Newell et al., 2004; Sotirelis et al., 2005). Sotirelis et al. (2005) showed that the correlation is best at dawn and dusk sectors, whereas, CRBs at dayside may have a large latitudinal jump at around noon (Y.-J. Chen et al., 2015; Koustov & Fiori, 2016). CRBs can be identified by locating a zero crossing in the latitudinal profile of the azimuthal component of the plasma flow (Bristow & Spaleta, 2013; Koustov & Fiori, 2016). We identify CRBs at three MLTs at dawn (5, 6, 7 hr) and three MLTs at dusk (17, 18, 19 hr). Using available SWBs and CRBs we then fit a least square circle to represent the OCB. This allows us to obtain a plasma flow profile perpendicular to the OCB at all local times at the dayside ionosphere. For OCB fitting, we require at least one reliable CRB at both dawn and dusk. On the dayside, depending upon the radar coverage, we can have SWBs from one or two radars. While we use all available SWBs on the dayside, we require SWBs to be available from at least two radar beams. A fitted circle in a geomagnetic coordinate system has been previously shown to be a simple yet practical construction for the polar cap boundary (Chisham, 2017; Holzworth & Meng, 1975; Meng et al., 1977; Pinnock et al., 2003).

On obtaining the circular OCB, we quantify the flow width by analyzing the longitudinal profile of the flow perpendicular to OCB one degree poleward of the fitted OCB at the dayside ionosphere. The northward component of the flow vectors is used to approximate the flow component perpendicular to OCB. The longitudinal profile is a nearly bell-shaped curve. Following Zou et al. (2019), we estimate the flow width using the Full Width at Half Maximum (FWHM) of the curve. Shay et al. (2003) followed an analogous approach in which the extremes of the reconnection X-line were identified based on an electron speed half of the peak value. Magnetopause reconnection rate is proportional to the plasma flow component perpendicular to the OCB (Chisham et al., 2008; Pinnock et al., 2003; Zou et al., 2021). Taking the FWHM excludes small magnitude flows around the tails of the profile where the flows are likely to be associated with a slow reconnection with sub-Alfvénic outflows (Zou et al., 2019). Therefore, the flow width we measure corresponds to a relatively fast merging region along the magnetopause. Although we primarily employ FWHM in our analysis, we also use constant threshold values 200 and 300 m/s to test if statistical results differ significantly. Radar LOS velocities with error estimations larger than 200 m/s are not used for fitting in the SHF method (Ruohoniemi & Baker, 1998). More uncertainty related to the LOS velocities is therefore included if threshold values lower than 200 m/s are used. Similarly, when threshold values more than 300 m/s are used, the technique is limited to instances with relatively stronger northward flows. The different threshold results are included in Supporting Information S1.

We measure the width of the flow channel associated with the magnetopause reconnection that the satellite detects. To establish the association, we test whether the satellite footprint lies within the ionospheric flow channel. We trace field lines from the satellite location to the ionosphere using the T89 (N. A. Tsyganenko, 1989) and T96 (N. Tsyganenko, 1995) magnetic field models. The satellite footprint must lie within the flow channel based on at least one model. For a reliable measurement of the flow width, we further require that the flow profile at the satellite footprint be defined by the fitted vectors modeled at actual radar measurement locations. This is possible when there is good radar coverage on the dayside ionosphere. We also use the LOS velocity measured by the radars to validate the fitted vectors. The calculated flow represents the azimuthal span of the flow channel

related to the reconnection that the satellites detect. It is worth noting that there could be additional flow channels in the ionosphere distinct from the one where the satellite footprint falls. They are deemed unassociated with the observed in situ counterparts. To obtain the length of the magnetopause reconnection X-line corresponding to the ionospheric flow channel, we perform field line tracing from the east and west boundaries of the ionospheric flow channel to the GSM- XY plane using the magnetospheric models. It is to be noted that we ignore the curvature of the magnetopause surface and only take the X-line extent in the GSM-Y direction to avoid additional uncertainties associated with the magnetospheric models.

4. Results and Discussion

4.1. Example Event 1: Spatially Extended Reconnection

On 4 May 2015, THEMIS-A observed reconnection during its outbound crossing near the subsolar magnetopause region ($X_{GSM} \sim 11.3$ RE, $Y_{GSM} \sim -0.4$ RE, $Z_{GSM} \sim -0.7$ RE) from ∼19:34 to ∼19:36 UT. The satellite observations during this magnetopause traversal are summarized in Figures 2b–2e. Figure 2b shows spin resolution (∼3 s) magnetic field data in the LMN coordinate system. The clear rotation B_L in Figure 2b accompanied by a change in ion energy spectra in Figure 2c indicates the magnetopause crossing. As shown in Figure 2e, the satellite detected fast northward-directed ions at the magnetopause boundary indicating possible reconnection outflow originating from a reconnection X-Line southward from the satellite location. The observed speed in the magnetopause boundary reached up to 306 km/s. We performed the Walen test and compared the observed speed with the theoretical prediction for a reconnection outflow. The vertical black line in Figures 2b–2e show the magnetosheath reference location. The dashed black curve in Figure 2e shows the speed profile predicted by the Walen relation. Although the observed speed is smaller than the predicted value during much of the boundary-crossing interval, the rotation in B_L is accompanied by the enhancement in V_L, and the criteria $\Delta V^* > 0.5$ is satisfied for ∼35% of the magnetopause crossing interval. At the location shown by the vertical red line where the observed speed is maximum and the magnetospheric density is larger than 20% of the magnetosheath value, the predicted and the observed jet speeds are ∼158 km/s and ∼124 km/s, respectively. The dimensional quantity ΔV^* is 0.52 indicating a reasonable agreement with the theoretical prediction. The earthward edge of the magnetopause has a relatively strong current sheet as indicated by a faster change in B_L. The appearance of strong V_M might be due to the strong current sheet being oriented differently from the overall current sheet. The magnetic shear angle is calculated as ∼127°. As shown in Figure 2e, plasma flows are much smaller on both sides of the magnetopause. This is usually expected at low latitude subsolar magnetopause.

Figures 2f–2l show the solar wind parameters measured by WIND at the L1 point. Plotted are the measurements propagated to the bow shock nose. As shown in Figure 2f, IMF was fairly stable in the interval preceding the reconnection event. The IMF had a dominant Bx component ($Bx/|\mathbf{B}| \sim 0.9$) with appreciable southward (negative Bz) and duskward (positive By) orientations until ∼4 min before THEMIS-A crossed the magnetopause boundary. The solar wind was relatively slow (∼350 km/s) with an Alfvén Mach number ∼6.5. The proton density and the dynamic pressure were ∼3.4 cm^{-3} and ∼0.7 nPa, respectively. Overall, the event was driven by modest solar wind conditions.

The concurrent SuperDARN observations at 19:36 UT are shown in Figures 2m–2o. As shown by the fitted velocity vectors in Figures 2m and 2o, the ionospheric plasma convected antisunward across the high latitude polar ionosphere and circulated back sunward along the lower latitude region which is a typical convection pattern during southward IMF conditions. At dayside, the plasma flow was strongly directed toward dawn, consistent with the expected flow for the positive IMF-By condition. Green circular markers at dawn and dusk sectors represent CRBs where plasma convection changes from sunward to antisunward. The radar scan in Figure 2m shows the Doppler spectral width measured by RKN and INV. We searched for SWBs on the eight most meridional beams of the radars. The black circles in the radar FOV represent the identified SWBs. The dashed circle represents the fitted OCB. As shown in Figure 2n, radars RKN and INV observed plasma flows in the direction away from the radar location. Note that, for plotting purposes, we have reversed the sign of LOS velocity so that positive values refer to the LOS velocity away from the radar location. This is different from the usual SuperDARN convention. As indicated by the "plus" markers, the satellite was mapped close to the FOVs of both radars. Figure 2o shows the longitudinal variation of the northward velocity component across the OCB. The profile is taken one degree poleward from the OCB. The circular markers along the line plot correspond to the data points with LOS velocity measurement. The vertical bars represent the standard deviation of the gridded velocity

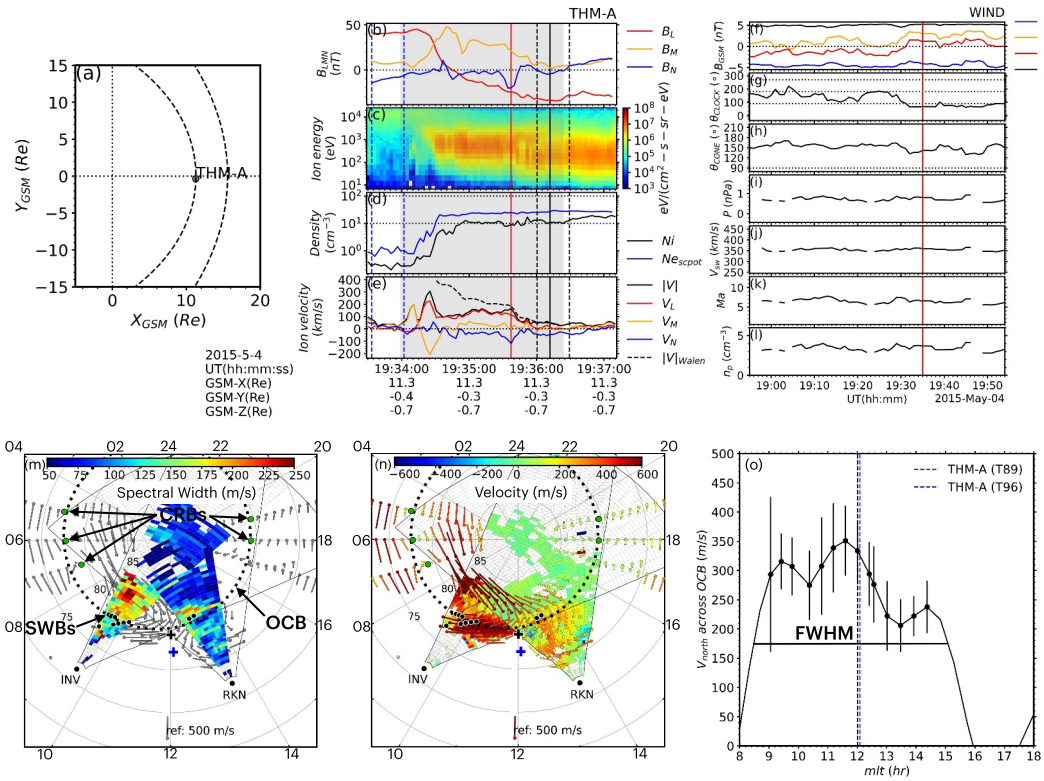

Figure 2. Overview of THEMIS-SuperDARN coordinated observation of a magnetopause reconnection event on 4 May 2015. (a) THEMIS-A location with modeled magnetopause and bow shock (Chao et al., 2002). (b–e) Summary of magnetopause observation showing (b) magnetic field in the LMN coordinate system, (c) ion energy spectra, (d) ion density, and (e) ion velocity in the LMN coordinate system. The dashed black line is the predicted velocity profile. The vertical line in black represents the magnetosheath reference location used in the Walen test. The vertical red line shows the magnetopause location with the maximum observed ion speed and a density above 20 percent of the magnetosheath value. The shaded region shows the magnetopause boundary interval. Vertical dashed lines in blue and black show the interval used to obtain the average plasma conditions in the magnetosphere and the magnetosheath adjacent to the boundary. (f–l) Solar wind parameters measured by WIND shifted to the bow shock showing (f) magnetic field, (g) IMF clock angle $\left(tan^{-1}[By/Bz]\right)$, (h) IMF cone angle $\left(cos^{-1}[Bx/|\mathbf{B}|]\right)$, (i) dynamic pressure, (j) solar wind speed, (k) Alfvén Mach number and (l) proton density. The vertical red line shows the time of jet detection by the satellite. (m) Radar scan of the Dopper spectral width and vectors showing SuperDARN fitted velocity in AACGM- MLT coordinate system. The fan-shaped outline represents the radar field of view. Spectral width is shown on the eight most meridional beams. Fitted vectors are shown at dawn (5, 6, and 7 hr MLTs) and dusk (17, 18, and 19 hr MLTs), and at dayside where there is radar coverage. Green circles at dawn and dusk delineate CRBs. Black circles in the radar field of view show SWBs. The dashed circle shows the fitted OCB. "Plus" markers in black and blue show the satellite footprint obtained using the T89 and T96 models, respectively. (n) Similar to (m) but the radar scans show the LOS velocities. Negative and positive values represent LOS velocity toward and away from the radar location, respectively. (o) Profile of the northward component of fitted vectors one degree poleward of the fitted OCB. The black circular markers indicate fitted velocity vectors at radar measurement locations and the error bars are the associated standard deviations (see text for the details). The horizontal line represents the FWHM. Vertical dashed lines in black and blue mark MLT of the satellite footprint obtained using T89 and T96 models.

at the given latitude/longitude cell, which is derived from the LOS velocity (Ruohoniemi & Baker, 1998). As shown by the vertical dashed lines, the satellite footprint conveniently falls within the longitudinal span of the flow structure. The FWHM of the flow profile was determined to be ~6.6 hr MLT. In the F region ionosphere, this corresponds to a flow width of ~1,729 Km. Using the T89 and T96 models, we projected the flow boundaries onto the GSM equatorial plane and calculated the X-line's length in the GSM-Y direction. The X-lines under T89 and T96 were ~19.5 RE and ~17.6 RE long, respectively.

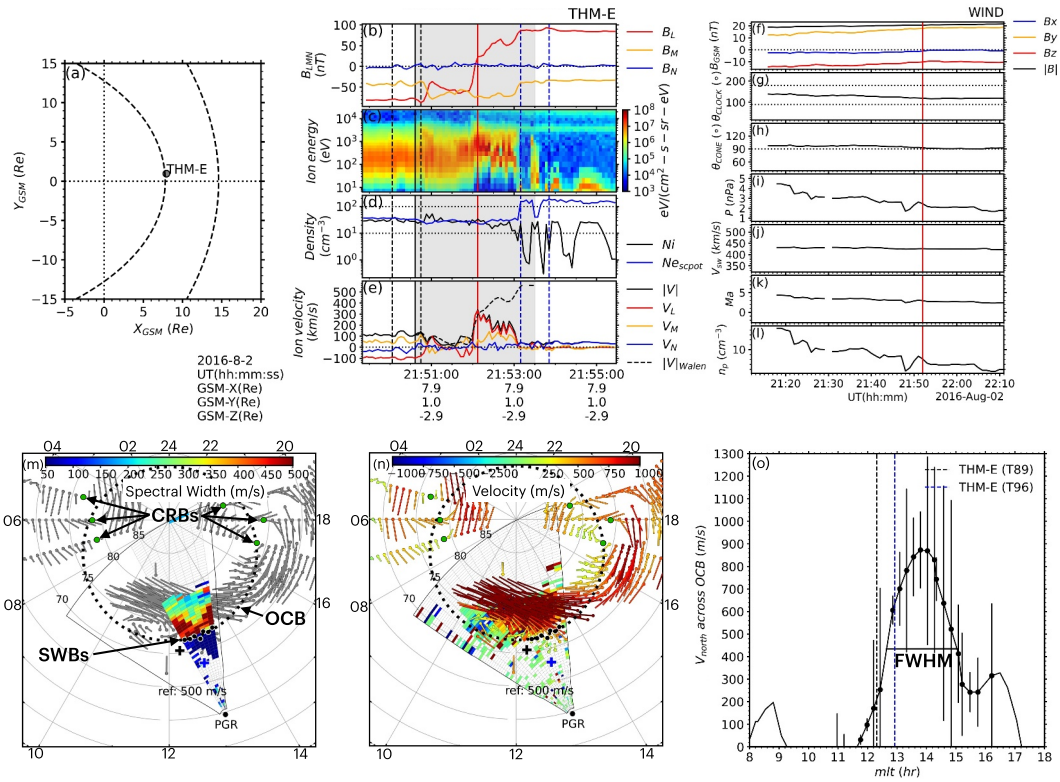

Figure 3. Overview of THEMIS-SuperDARN coordinated observation of a magnetopause reconnection event on 2 August 2016. The layout is similar to Figure 2.

4.2. Example Event 2: Spatially Patchy Reconnection

On 2 August 2016, THEMIS-E recorded a reconnection event at the subsolar magnetopause during its inbound pass near the sub-solar region (X_{GSM} ~ 7.9 RE, Y_{GSM} ~ 1.0 RE, Z_{GSM} ~ −2.9 RE) between ~20:51 UT and ~20:53 UT. The fast northward ions at the magnetopause boundary, as depicted in Figure 3e, indicates a reconnection outflow originated at the reconnection X-Line southward from the satellite location. The satellite observed a peak plasma speed of almost 340 km/s. At the peak, the observed change in the jet speed closely matched the theoretical prediction by the Walen relation. The angle between the predicted and the observed jets was ~18°. Unlike the previous event, the magnetospheric side of the magnetopause was populated with low-energy ions (Figure 3c). As the density profiles in Figure 3d show, ESA ion density (black curve) increased in the magnetospheric area, reaching up to ~30 cc^{-3}. Moreover, the density including the lower energy plasma (blue curve) reached over 100 cc^{-3}. As shown in Figure 3e, the satellite also observed significant flow in the magnetosheath side of the boundary. The plasma flow in the L direction was ~−100 km/s. The significant southward flow is not surprising because the satellite crossed the magnetopause ~2.9 RE below the equatorial plane. Considering relatively stationary magnetospheric plasma and the detection of the northward jets, the magnetosheath flow near the X-line region is predicted to be even larger. The magnetic shear angle was ~163°.

Figure 3f shows that the IMF was remarkably steady with strong southward and duskward components (Clock angle ~130°). For IMF with significant By component, a tilted component reconnection X-line is predicted to run along the subsolar magnetopause that shifts southward in the summer months due to the dipole tilt effect (Hoshi et al., 2018; Trattner et al., 2007). The overall picture is therefore consistent with the prediction. Solar wind speed was steady at ~430 km/s. The Alfvén mach number was ~3.5. The proton number density was ~9 cm^{-3}.

Figures 3m–3o show the SuperDARN observations at 21:54 UT. The fitted vectors in Figures 3m and 3n show highly enhanced dawnward directed flows, consistent with the anticipated flow in the case of strongly positive IMF-By condition. Figure 3m displays the Doppler spectral width measured by PGR. SWB is identified in all of the near meridional beams. The magnetic latitudes of the SWBs are between ~72°and ~73°, which shows that the

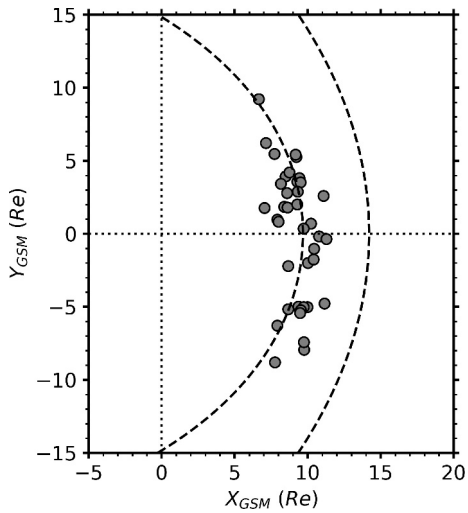

Figure 4. Locations of THEMIS satellites on the GSM-XY plane along with a modeled magnetopause and bow shock (Chao et al., 2002).

polar cap size was relatively larger in this case. As shown in Figure 3o, the FWHM of the antisunward flow channel is ∼2.4 hr MLT. This represents a relatively narrow azimuthal extent. This corresponds to a flow width of ∼1,064 km in the F region ionosphere. The estimated lengths of the X-line in the GSM-Y direction under T89 and T96 were ∼6.5 RE and ∼8.3 RE, respectively.

4.3. Statistical Study

We surveyed 3 years (2015–2017 inclusive) of dayside magnetopause crossing events by THEMIS A, D, and E. Candidate reconnection events were identified based on satellite detection of fast ion flows at the magnetopause boundary. On confirming the in situ reconnection using the Walen test, we analyzed SuperDARN observation in the northern hemisphere to select the cases with a clear detection of the ionospheric counterpart of the reconnection. Following the procedure described in the methodology section, we attempted to measure the width of the reconnection-driven antisunward flow channels. We finally compiled 39 event cases with clear in situ reconnection signatures and simultaneous determination of the associated flow width in the ionosphere. Our event list also includes two 2015 events detailed by Zou et al. (2019). Zou et al. (2019) used velocity vectors constructed from the Spherical Elementary Current Systems (SECS) (Amm et al., 2010) method to obtain the FWHM of the ionospheric flow profiles. The changes in the methodology did not result in significant differences in the flow widths for the 29 April event (Event 16 in the current list). However, the flow widths differed significantly for the 19 April event (Event 14 in the current list), which is mainly because of the sensitivity of the width defined by FWHM on the flow maximum speed. The SECS approach in Zou et al. (2019) produced a peak antisunward speed about twice as large as the SHF approach in this work, resulting in the FWHM being much narrower. A rough estimation shows that the flow widths for this event from the two approaches do not differ significantly if a constant threshold is used instead of FWHM. Figure 4 shows the spatial distribution of the satellites on the GSM-XY plane. The dashed lines represent the model magnetopause and the bow shock (Chao et al., 2002) obtained for average conditions.

The reconnection time stamp was taken for each event where the satellite recorded the peak outflow speed. SuperDARN provides fitted velocity vectors with a temporal resolution of 2 min. We measured the flow width for the three consecutive SuperDARN observations starting from the reconnection time and took the average of the three values as the ionospheric measure. The estimates deemed inaccurate due to an unreliable OCB or significant data gaps in the ionospheric velocity profile were excluded from averaging. Figure 5 shows histograms of the three quantities characterizing the spatial extent of the reconnection structures. Figure 5a shows the azimuthal extent of the ionospheric flow channel in the AACGM MLT. This also represents the azimuthal extent of the reconnection X-line on the magnetopause. A wide variation in the azimuthal extent ranging from ∼1.5 hr MLT to

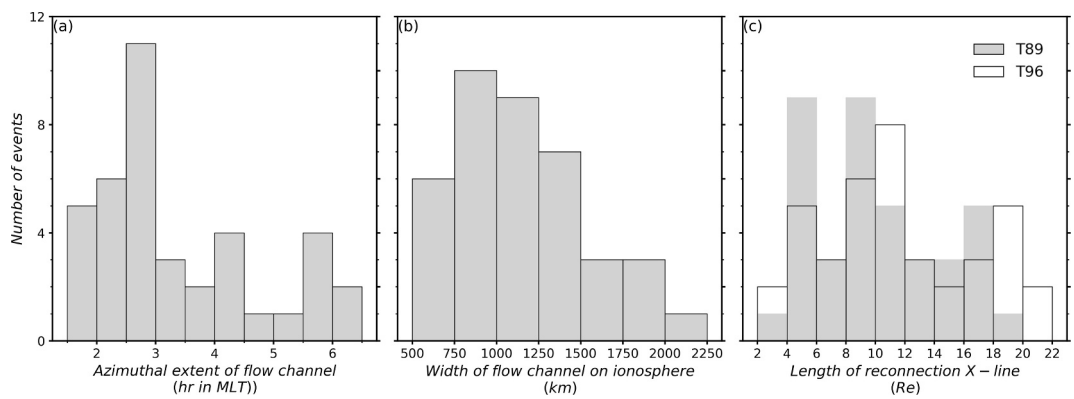

Figure 5. Histograms showing (a) the azimuthal extent of the flow channels in MLT, (b) the width of the flow channels on the ionosphere, and (c) the length of the reconnection X-lines in the GSM-Y direction.

~6.5 hr MLT is recorded. Figure 5b shows the width of the flow channels in the F-region ionosphere. We measured the flow channels to be as narrow as ~600 km and as wide as ~2,200 km. Figure 5c shows the estimated length of magnetopause reconnection X-line in the GSM-Y direction. To obtain this, we traced the magnetic field lines from the ionospheric flow boundaries to the GSM equatorial plane using the T89 and T96 models and took the extent in the GSM-Y direction. Notably different outcomes are obtained from the two models, and the discrepancies for the extended events are found to be relatively large. We recorded a maximum difference of ~5.5 Re. In some events when the OCB latitudes were relatively higher on the dayside, the geomagnetic field lines either remained open or stretched backward (antisunward) before closing on the southern hemisphere. In such cases, we considered the nearest field lines at the same longitude that closed without the backward stretching. In practice, we repeatedly performed the mapping reducing the flow boundary latitude by 0.1° each time until the desirable configuration was achieved. Reductions of as much as 6° were needed for our events. It has to be noted that the estimates of the X-lines thus obtained most likely represent the lower limit. We found that the magnetopause reconnection X-lines can range from ~3 RE to ~22 RE in the GSM-Y direction. We emphasize that the length estimates of the reconnection X-line should be used mainly for illustrative purposes due to the significant uncertainties involved in the tracing method. The results are best interpreted in terms of the AACGM MLT.

The differences in the shapes of the three distributions in Figure 5 are expected. For two events with the same azimuthal extent in MLT, one with a larger polar cap (OCB on lower latitude) will have a wider flow on the ionosphere, and one with the larger magnetosphere will have a longer X-line along the magnetopause. In the following statistical study, we focus only on the azimuthal span of reconnection in the "hr MLT" unit owing to its direct relevance with the spread of the reconnection line along the local time and comparatively less calculation uncertainty.

To investigate the possible factors controlling the azimuthal span of magnetopause reconnection, we studied both local magnetopause conditions and the solar wind-driving conditions upstream of the bow shock. We used ACE and WIND data sets shifted to the bow shock. When data from both monitors were available, we selected the upstream monitor closer to the Sun-Earth line for more representative solar-wind conditions. For most cases, the differences between the ACE and WIND measurements were insignificant. When ACE and WIND were located on the different GSM-Y direction about the Sun-Earth line and a discrepancy existed in the IMF-Bz component, the monitor observing stronger southward IMF (negative Bz) was chosen taking into account the THEMIS observations of magnetopause reconnection at the low-latitude magnetopause on the dayside.

The solar wind conditions were obtained by averaging a 20-min interval before the reconnection time stamp. The averaging period of 20 min compasses the propagation time from the bow shock to the magnetopause, which is often assumed to be several minutes. The majority of our events (26 out of 39) exhibit generally stable IMF orientations throughout the averaging interval. Among these, seven events show minimal variations, with standard deviations below 0.5 nT for all three IMF components. Eleven events have at least one component with a standard deviation greater than 0.5 nT but less than 1 nT. In the remaining eight events, at least one component shows a standard deviation greater than 1 nT, although none of the components changes sign during the averaging interval. It must be noted that sign changes are disregarded when a component remains predominantly positive or negative, with minor excursions (less than 2 nT) across the axis, as the averaged value reflects the overall condition. Certain events were excluded from the analysis based on visual identification of rapidly fluctuating IMF components over the averaging interval.

The local plasma conditions from THEMIS were obtained by averaging 10 data points (~30 s) immediately outside the magnetopause boundary which is often characterized by variations in magnetic field and ion velocity as well as a mixing of magnetosheath and magnetospheric plasma population. In some cases, when the satellites observed the magnetosphere or magnetosheath for less than 30 s, the available interval was averaged.

In Figure 6, the flow width in MLT is plotted against several solar wind parameters namely, clock angle, cone angle, solar wind speed, and Alfvén Mach number. The IMF orientation (Zou et al., 2019) and solar wind flow characteristics (Borovsky, 2013; S. E. Milan et al., 2016) were previously suggested to be important controlling factors. We also investigated possible relationships with additional solar wind parameters such as proton density, plasma beta, and temperature, and no obvious association was observed (plots not shown). The error bars represent the range of FWHM of the flow channels calculated considering the error bars along the velocity profiles (Figures 2o and 3o). The given error values at each location along the velocity profile are averaged to

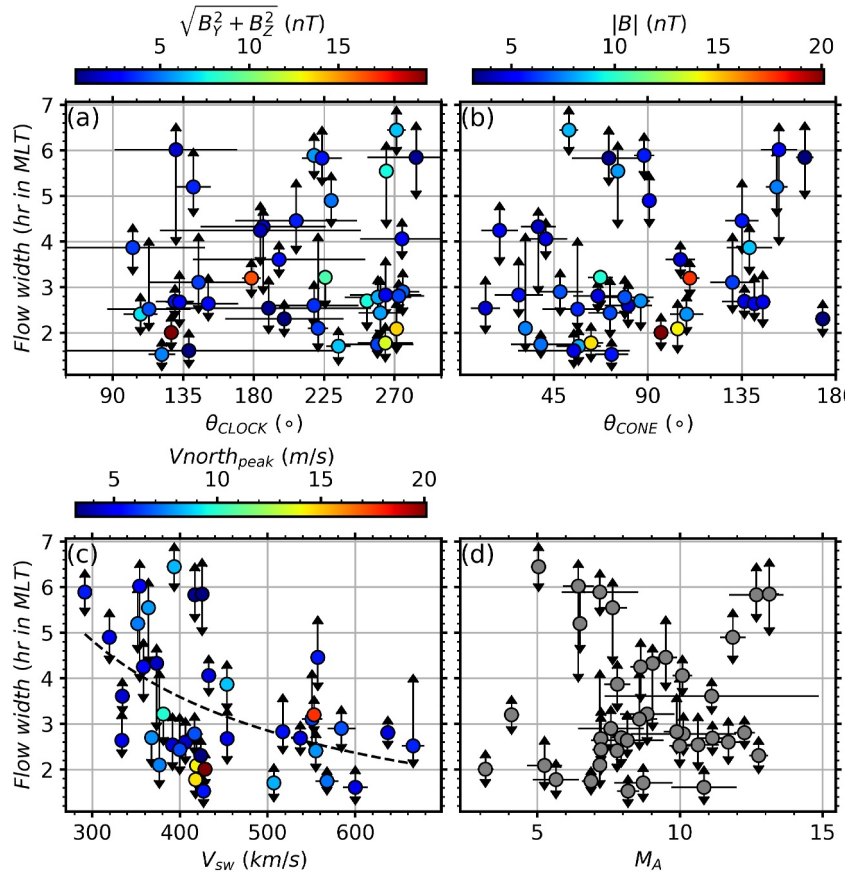

Figure 6. Flow width plotted against the solar wind parameters: (a) IMF clock angle color coded by the strength of IMF projected on GSM-YZ plane; (b) IMF cone angle color coded by IMF total strength; (c) solar wind speed color coded by peak northward ionospheric flow. The dashed line shows the power law fit (prefactor = 1905 and exponent = −1.05), and (d) solar wind Alfvén Mach number. The error bars along the horizontal direction represent the standard deviation of the independent variables in the averaging interval.

obtain a mean error. The upper/lower value of the FWHM is then estimated by calculating the FWHM of a new curve that is defined by adding or subtracting the mean error to/from each value along the original curve.

Figure 6a shows the IMF clock angle on the horizontal axis. Clock angle is defined as $\left(\tan^{-1}[\mathrm{By}/\mathrm{Bz}]\right)$ representing the angle between the IMF projection on the GSM-YZ plane and the GSM-Z axis. The data points are color-coded according to the magnitude of the IMF projection on the GSM-YZ plane, which together with the clock angle, provides information on the relative strength of By and Bz components. Clock angles of 0° and 180° represent purely northward ($\mathrm{Bz} > 0, \mathrm{By} = 0$) and purely southward ($\mathrm{Bz} < 0, \mathrm{By} = 0$) IMF, respectively. Similarly, clock angles of 90° and 270° represent purely duskward ($\mathrm{Bz} = 0, \mathrm{By} > 0$) and purely dawnward ($\mathrm{Bz} = 0, \mathrm{By} < 0$) IMF, respectively. With a few exceptions, most events have clock angles between 90° and 270°, reflecting average IMF conditions with a southward component (IMF-Bz < 0). This is usually expected for dayside magnetopause reconnection near the subsolar region. While we do not see an obvious trend with clock angle, for events with purely southward IMF conditions (near 180°), the flow widths fall in a narrow intermediate range (∼2 hr MLT to ∼5 hr) in MLT. With increasing dawnward or duskward components of IMF (away from 180°), flow widths are observed over a wider range. However, for events with strongly dawnward or duskward IMF (data points away from 180° with high color bar values), the flow widths are comparatively narrow ∼2 hr MLT. For the majority of those cases, the flow widths based on the thresholds 200 and 300 m/s are also relatively narrow (see Figures S1 and S2 in Supporting Information S1). Strong IMF-By drives the antisunward flow with a greater azimuthal component on the dayside ionosphere (Heelis, 1984; Thomas & Shepherd, 2018). Consequently, the width of the northward flow channel measured across the circular OCB tends to be narrower. It is

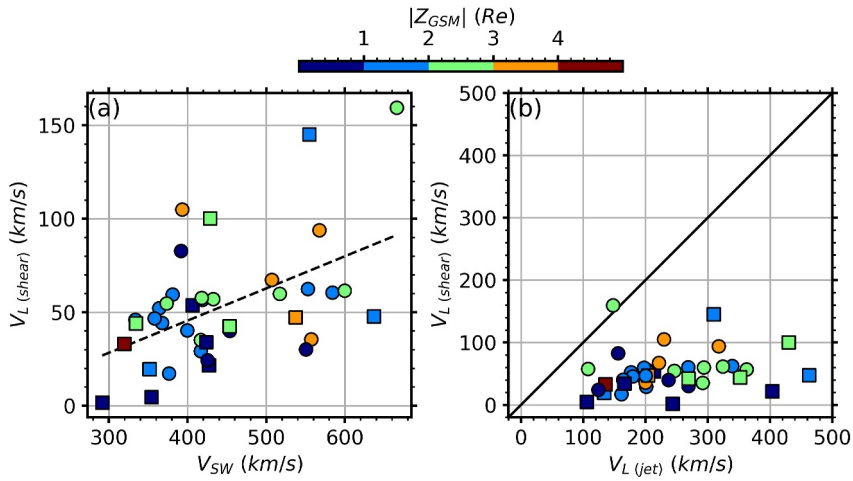

Figure 7. (a) Velocity shear in the L direction plotted against solar wind speed. The dashed line represent the line of best fit. (b) Velocity shear in the L direction plotted against jet speed in the L direction. Colorbar represents the absolute value of GSM-Z location of the magnetopause observation. The square markers represent the cases in which the satellites are either in the northern hemisphere detecting the southward jet or the southern hemisphere detecting the northward jet.

worth mentioning that with the use of a smooth circular OCB, any effects arising due to significant tilting of the dayside OCB (if present) could not be considered.

Figure 6b shows the IMF cone angle on the X-axis. The IMF cone angle is defined as $\left(\cos^{-1}[\mathrm{Bx}/|\mathbf{B}|]\right)$ that represents the angle between IMF direction and the sun-earth line. The data points are color-coded by magnetic field strength. Cone angles of 0° and 180° represent purely sunward and earthward IMF, respectively. Cone angles below 45° and above 135° are typically considered dominant Bx conditions. We do not see an appreciable difference between sunward (cone angle <90) and earthward (cone angle >90) directed IMF conditions concerning the azimuthal extent of reconnection. About 41% of our events are observed during dominant Bx conditions in which we see both narrow and extended events. All events with strong magnetic field strength (|B| > 10 nT) have comparatively narrow flow widths. However, the number of events in this category is limited.

In Figure 6c, the flow width is plotted as a function of solar wind speed. The data points are color coded according to the peak of the ionospheric flow profiles (see panel (o) in Figures 2 and 3). The first observation is that the flow width is inversely proportional to the solar wind speed (also see Figures S1 and S2 in Supporting Information S1). Most extended events are observed during lower solar wind speed conditions, whereas the flow channels are mostly narrow during higher solar wind speeds. Another feature of Figure 6c is that the northward flow is positively correlated with the solar wind speed. Interestingly, the ionospheric flows during high solar wind speed conditions are narrower but stronger.

A negative association of flow width with solar wind was also previously reported by Zou et al. (2019). One probable explanation is based on the effect of flow shear at the magnetopause boundary. Magnetopause reconnection rate is suggested to fall off with increasing plasma flow shear (jump) across the magnetopause boundary (Cassak & Otto, 2011; Q. Chen et al., 1997; Mitchell & Kan, 1978). The reconnection rate is suggested to drop by 30% when the flow shear is equal to the local Alfvén speed and completely stop when the flow shear is twice the Alfvén speed (Cassak & Otto, 2011).

The magnetosheath flow increases with both upstream solar wind speed and the distance from the magnetopause nose. A positive association ($r \sim 0.5$) between solar wind speed and the velocity shear in L direction in Figure 7a indicates that solar wind speed contributes to velocity shear in the direction of the reconnecting magnetic field. However, the association is less obvious at higher values of solar wind speed. The average velocity shear is ~54 km/s with values as large as ~159 km/s. In Figure 7, the square markers are used for the events when the satellites are either in the northern hemisphere detecting the southward jet or the southern hemisphere detecting the northward jet. In both scenarios, the X-lines ought to be farther than the satellites from the equatorial plane. Considering the increased magnetosheath flow, the velocity shear near the X-lines is expected to be larger than the values recorded by the satellites. We observed X-lines at least ~4.4 RE below the equatorial plane and up to ~3.7

RE above the equatorial plane based on the direction of the observed jets. For southward IMF conditions with notable IMF-By component (a condition usually in reality), the component reconnection X-line near the sub-solar region are found to shift by up to ∼6 RE toward the winter hemisphere (Hoshi et al., 2018). These conditions might lead to increased flow shear across the X-line.

In Figure 7b, the velocity shear values are compared with the jet speeds. As expected for an active reconnection, most shear values are smaller than the jet speed. However, a few data points are fairly close to the identity line. With increasing distance from the magnetopause nose along the X-line, the shear values may increase due to the faster magnetosheath flow. The combined effect of high solar wind speed and the increased distance of X-lines from the equatorial plane might lead to high velocity shear at certain regions along the X-lines. However, with our observational limitations, it is not possible to determine whether or not the velocity shear acts to limit the span of X-line.

The possible effect of velocity shear in constraining the X-line on the dayside was previously studied by Borovsky (2013). A critical condition in terms of Alfvén Mach number (M_A) of the magnetosheath flow and the magnetosheath plasma beta was formulated for an effective X-line length (Borovsky, 2013, Equation 12). The central idea in the formulation was that the effective length of the X-line is determined based on the location where the flow speed in the magnetosheath is equal to the local Alfvén speed. Using simulation, it was shown that the azimuthal extent of reconnection X-line is proportional to $M_A^{-0.404}$. As shown in Figure 6d, such a power law relationship is not evident in our data. In the simulation, (M_A) was varied over a wide range (∼2 to ∼40) according to magnetic field strength while keeping solar wind density and speed constant, whereas most of our events have M_A in an intermediate range (6–13) with highly variable solar wind density and speed.

We note that there may be other physical mechanisms that account for the observed association with solar wind speed. For example, high solar wind speed conditions favor the development of the localized high dynamic pressure pulses in the magnetosheath (also called the magnetosheath jets) (LaMoury et al., 2021). By changing the local magnetic field and plasma properties, the jets have the potential to modulate the magnetopause reconnection (Hietala et al., 2018; Ng et al., 2021; Vuorinen et al., 2021). During southward IMF conditions, jets can impact the local reconnection by introducing northward IMF at the magnetopause (Vuorinen et al., 2021), potentially resulting in patchy reconnection sites.

We investigated possible effect of the magnetospheric density on the length of the reconnection X-line. The dayside magnetosphere near the subsolar magnetopause typically has high energy plasma with densities $\sim 0.1 \mathrm{cm}^{-3}$. However, the region is often dominated by dense cold plasma of ionospheric origin. Due to the dependence of the local Alfvén speed on the densities on either side of the magnetopause (Birn et al., 2008; Cassak & Shay, 2007), magnetospheric ions can significantly reduce the magnetopause reconnection rate and the outflow speed. It has been postulated that magnetopause reconnection under such conditions is more susceptible to suppression due to the velocity shear effect, potentially leading to shorter X-lines (Borovsky, 2013; Borovsky et al., 2013).

The bulk of the cold magnetospheric plasma has energy below the lower energy threshold of the ESA instrument. Therefore, we computed density using the spacecraft potential measured by the EFI instrument. Figure 8a shows the magnetopause crossing locations color-coded by the magnetospheric electron density. With a few exceptions, high-density measurements are preferentially clustered in the post-noon sector toward dusk. The region is where plasmaspheric plume drainage is typically found to occur (André & Cully, 2012; Borovsky & Denton, 2006, 2008; McFadden, Carlson, Larson, Bonnell, et al., 2008; Walsh et al., 2013). In Figure 8b, the ionospheric flow width is plotted against the magnetospheric density. Although a limited number of events with very high magnetospheric density ($\geq$30 cm^{-3}) have a relatively narrow reconnection span, no overall trend is seen. Zou et al. (2021) showed that dense ($\geq$20 cm^{-3}) plumes resulted in suppression of ionospheric flow at the MLT where the plumes contacted the magnetopause. However, the ionospheric flow in the region adjacent to the plumes were shown to increase. Also, it has to be noted that the impact of the cold ions on magnetopause reconnection may also depend on the spatial extent of the cold ion population, which can be a fraction of RE or many RE's (Borovsky & Denton, 2008; Nishimura et al., 2022). In Figure 8b, data points exhibit significant diversity in the geomagnetic conditions, as indicated by the colors based on the geomagnetic Kp index.

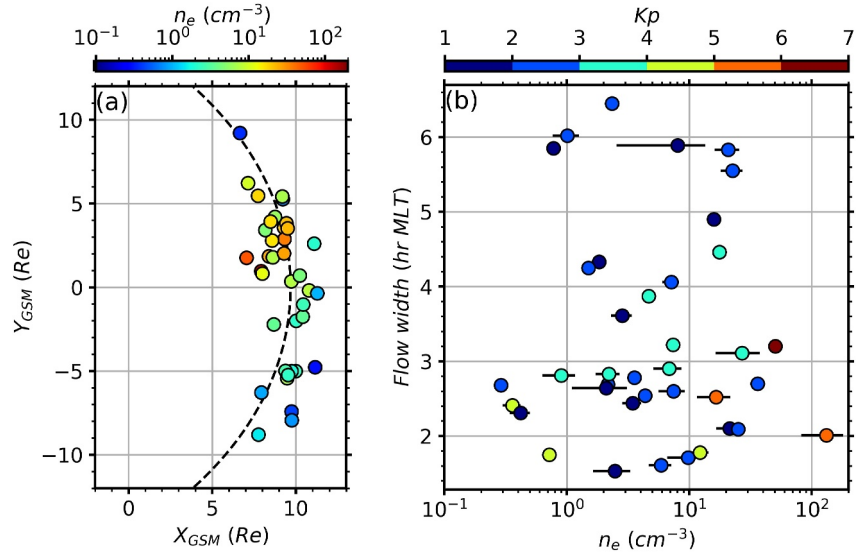

Figure 8. (a) Distribution of satellites on GSM- XY plane. The color bar represents magnetospheric electron density. The dashed line represents the nominal magnetopause. (b) Ionospheric flow width plotted against the magnetospheric electron density. The color bar shows the geomagnetic Kp index.

4.3.1. Uncertainties and Limitations

The spacing of SuperDARN fitted vectors is ∼111 km in the ionosphere. This corresponds to an azimuthal resolution of ∼0.3 hr MLT at the magnetic latitude 78° around where most SWBs are identified. Therefore, any discontinuities in the flow channels below that resolution can not be identified. Additionally, this places a lower limit of ∼0.6 hr MLT (three data points) on the flow width measurement. The measured azimuthal span of the ionospheric flow channels corresponds to the portion of dayside magnetopause where open field lines are created. However, we cannot distinguish if the ionospheric flow channels are driven by reconnection along a single X line or multiple X-lines that may exist at the magnetopause (Fuselier et al., 2011, 2017, 2018; Hasegawa et al., 2010; Vines et al., 2017). We presented an analysis using a threshold of 150 m/s for SWB determination. To examine the effect of using different thresholds, we repeated our analyses using higher thresholds 180 and 210 m/s. As expected, higher thresholds did not work for events with relatively low amplitude distribution of spectral width. For analysis based on FWHM, thresholds 180 and 210 m/s worked well in 37 and 34 of our events, respectively. We determined that our results are not significantly sensitive to the threshold used. The events were identified in the UT range of 15:30 to 22:30 owing to favorable radar coverage on the dayside ionosphere. Similarly, most (∼87%) of our events fell in the spring equinox- summer months, and no events were sampled from the winter months. Therefore, bias may exist in the distribution of the local time extent of reconnection due to seasonal and UT effects (if any).

4.4. Summary and Conclusions

By leveraging the remote sensing capability of SuperDARN, we studied 39 magnetopause reconnection events and attempted to address the question: What is the spatial extent of magnetopause reconnection, and what controls it? For each magnetopause reconnection event detected by THEMIS, we identified the corresponding antisunward flow channel in the ionosphere and measured the flow width just inside the OCB. In this statistical study, we showed that magnetopause reconnection can have a wide variability in azimuthal extent from ∼1.5 hr MLT to ∼6.5 hr MLT, corresponding to magnetopause reconnection X-lines of a few RE to ∼22 RE long in the GSM-Y direction.

We investigated the solar wind driving conditions with particular emphasis on IMF orientations and flow speed. Our results showed that higher solar wind speed are associated with shorter X-lines but stronger ionospheric flow across the OCB. As a probable explanation, we discussed the potential importance of velocity shear in limiting the X-line length (Borovsky, 2013; Borovsky et al., 2013). Assuming dayside reconnection occurs along the equatorial plane, the velocity shear effect on the dayside magnetopause reconnection is often deemed unimportant

because the magnetosheath bulk flow is dominantly in the direction perpendicular to the reconnection plane (Doss et al., 2015; Komar et al., 2015). Our observations showed that solar wind flow may introduce notable velocity shear in the direction of reconnected magnetic field. However, to conclusively determine whether or not velocity shear actually plays a role to limit the span of X-line, we require unambiguous measurements of the velocity shear across the X-lines at different local times. Multiple satellites simultaneously detecting the X-lines at different MLTs could ideally provide a better understanding of the mechanism.

We did not observe obvious effects due to solar wind IMF orientations. However, for a limited number of events observed under dominant IMF-By conditions, reconnection was azimuthally narrow possibly due to the plasma flow with high azimuthal but low normal components. We also investigated the possible role of magnetospheric cold ions contacting the dayside magnetopause. By lowering the local Alfvén speed, magnetospheric cold ions could make the dayside reconnection susceptible to the flow shear effect as the shear values are more likely to surpass the jet speeds. However, we did not observe any obvious trend with the magnetospheric density.

Data Availability Statement

SuperDARN data for individual radars were obtained from https://superdarn.ca (Greenwald, 1995). SuperDARN map data are available at https://zenodo.org/records/13336854 (Khanal, 2024). THEMIS Level 2 data were obtained from http://themis.ssl.berkeley.edu/ (Angelopoulos, 2009a). The ACE and WIND data were obtained from the GSFC/SPDF OMNIWeb interface at https://omniweb.gsfc.nasa.gov (Papitashvili & King, 2020). pyDARN is available at https://doi.org/10.5281/zenodo.13694617 (Shi et al., 2022). Matplotlib is available at https://doi.org/10.5281/zenodo.14464227 (Hunter, 2007). PySpedas is available at https://github.com/spedas/pyspedas (Grimes et al., 2022). SPEDAS is available at https://spedas.org/ (Angelopoulos et al., 2019).

Acknowledgments
The work is supported by the National Science Foundation under Grant 2025570. XS was supported by NSF awards AGS-2025570, AGS-1935110, and AGS-2307205. We acknowledge the use of SuperDARN data. SuperDARN is a network of radars funded by the national scientific funding agencies of Australia, Canada, China, France, Italy, Japan, Norway, South Africa, the United Kingdom, and the United States of America. We acknowledge NASA contract NAS5-02099 and V. Angelopoulos for the use of data from the THEMIS Mission. We acknowledge the use of ACE and WIND data from GSFC/SPDF OMNIWeb. We acknowledge the use of the Matplotlib, pyDARN, PySpedas, and SPEDAS packages for data analysis.

References

Amm, O., Grocott, A., Lester, M., & Yeoman, T. K. (2010). Local determination of ionospheric plasma convection from coherent scatter radar data using the secs technique. *Journal of Geophysical Research*, *115*(A3), A03304. https://doi.org/10.1029/2009ja014832

André, M., & Cully, C. M. (2012). Low-energy ions: A previously hidden solar system particle population. *Geophysical Research Letters*, *39*(3), L03101. https://doi.org/10.1029/2011gl050242

Angelopoulos, V. (2009a). THEMIS level 2 data [Dataset]. *THEMIS Science Operations Center (SOC)*. http://themis.ssl.berkeley.edu

Angelopoulos, V. (2009b). *The THEMIS mission*. Springer.

Angelopoulos, V., Cruce, P., Drozdov, A., Grimes, E., Hatzigeorgiu, N., King, D., et al. (2019). The space physics environment data analysis system (SPEDAS). *Space Science Reviews*, *215*, 1–46. https://doi.org/10.1007/s11214-018-0576-4

Atz, E. A., Walsh, B. M., Broll, J. M., & Zou, Y. (2022). The spatial extent of magnetopause magnetic reconnection from in situ themis measurements. *Journal of Geophysical Research: Space Physics*, *127*(12), e2022JA030894. https://doi.org/10.1029/2022ja030894

Auster, H., Glassmeier, K., Magnes, W., Aydogar, O., Baumjohann, W., Constantinescu, D., et al. (2008). The themis fluxgate magnetometer. *Space Science Reviews*, *141*, 235–264. https://doi.org/10.1007/978-0-387-89820-9_11

Baker, K., Dudeney, J., Greenwald, R., Pinnock, M., Newell, P., Rodger, A., et al. (1995). HF radar signatures of the cusp and low-latitude boundary layer. *Journal of Geophysical Research*, *100*(A5), 7671–7695. https://doi.org/10.1029/94ja01481

Baker, K., Rodger, A., & Lu, G. (1997). HF-radar observations of the dayside magnetic merging rate: A geospace environment modeling boundary layer campaign study. *Journal of Geophysical Research*, *102*(A5), 9603–9617. https://doi.org/10.1029/97ja00288

Birn, J., Borovsky, J., & Hesse, M. (2008). Properties of asymmetric magnetic reconnection. *Physics of Plasmas*, *15*(3). https://doi.org/10.1063/1.2888491

Bonnell, J., Mozer, F., Delory, G., Hull, A., Ergun, R., Cully, C., et al. (2009). The electric field instrument (EFI) for THEMIS. *The THEMIS Mission*, 303–341. https://doi.org/10.1007/978-0-387-89820-9_14

Borovsky, J. E. (2013). Physics-based solar wind driver functions for the magnetosphere: Combining the reconnection-coupled MHD generator with the viscous interaction. *Journal of Geophysical Research: Space Physics*, *118*(11), 7119–7150. https://doi.org/10.1002/jgra.50557

Borovsky, J. E., & Denton, M. H. (2006). Effect of plasmaspheric drainage plumes on solar-wind/magnetosphere coupling. *Geophysical Research Letters*, *33*(20), L20101. https://doi.org/10.1029/2006gl026519

Borovsky, J. E., & Denton, M. H. (2008). A statistical look at plasmaspheric drainage plumes. *Journal of Geophysical Research*, *113*(A9), A09221. https://doi.org/10.1029/2007ja012994

Borovsky, J. E., Denton, M. H., Denton, R. E., Jordanova, V. K., & Krall, J. (2013). Estimating the effects of ionospheric plasma on solar wind/magnetosphere coupling via mass loading of dayside reconnection: Ion-plasma-sheet oxygen, plasmaspheric drainage plumes, and the plasma cloak. *Journal of Geophysical Research: Space Physics*, *118*(9), 5695–5719. https://doi.org/10.1002/jgra.50527

Borovsky, J. E., Hesse, M., Birn, J., & Kuznetsova, M. M. (2008). What determines the reconnection rate at the dayside magnetosphere? *Journal of Geophysical Research*, *113*(A7), A07210. https://doi.org/10.1029/2007ja012645

Bristow, W., Hampton, D., & Otto, A. (2016). High-spatial-resolution velocity measurements derived using local divergence-free fitting of superdarn observations. *Journal of Geophysical Research: Space Physics*, *121*(2), 1349–1361. https://doi.org/10.1002/2015ja021862

Bristow, W., & Spaleta, J. (2013). An investigation of the characteristics of the convection reversal boundary under southward interplanetary magnetic field. *Journal of Geophysical Research: Space Physics*, *118*(10), 6338–6351. https://doi.org/10.1002/jgra.50526

Cassak, P., & Otto, A. (2011). Scaling of the magnetic reconnection rate with symmetric shear flow. *Physics of Plasmas*, *18*(7). https://doi.org/10.1063/1.3609771

Cassak, P., & Shay, M. (2007). Scaling of asymmetric magnetic reconnection: General theory and collisional simulations. *Physics of Plasmas*, *14*(10). https://doi.org/10.1063/1.2795630

Chao, J., Wu, D., Lin, C.-H., Yang, Y.-H., Wang, X., Kessel, M., et al. (2002). Models for the size and shape of the Earth's magnetopause and bow shock. In *Cospar colloquia series* (Vol. 12, pp. 127–135). https://doi.org/10.1016/s0964-2749(02)80212-8

Chen, Q., Otto, A., & Lee, L. (1997). Tearing instability, Kelvin-Helmholtz instability, and magnetic reconnection. *Journal of Geophysical Research*, *102*(A1), 151–161. https://doi.org/10.1029/96ja03144

Chen, Y.-J., Heelis, R., & Cumnock, J. (2015). Response of the ionospheric convection reversal boundary at high latitudes to changes in the interplanetary magnetic field. *Journal of Geophysical Research: Space Physics*, *120*(6), 5022–5034. https://doi.org/10.1002/2015ja021024

Chisham, G. (2017). A new methodology for the development of high-latitude ionospheric climatologies and empirical models. *Journal of Geophysical Research: Space Physics*, *122*(1), 932–947. https://doi.org/10.1002/2016ja023235

Chisham, G., & Freeman, M. (2003). A technique for accurately determining the cusp-region polar cap boundary using SuperDARN HF radar measurements. *Annales Geophysicae*, *21*(4), 983–996. https://doi.org/10.5194/angeo-21-983-2003

Chisham, G., & Freeman, M. (2004). An investigation of latitudinal transitions in the SuperDARN Doppler spectral width parameter at different magnetic local times. *Annales Geophysicae*, *22*(4), 1187–1202. https://doi.org/10.5194/angeo-22-1187-2004

Chisham, G., Freeman, M., Abel, G., Lam, M., Pinnock, M., Coleman, I., et al. (2008). Remote sensing of the spatial and temporal structure of magnetopause and magnetotail reconnection from the ionosphere. *Reviews of Geophysics*, *46*(1), RG1004. https://doi.org/10.1029/2007rg000223

Chisham, G., Freeman, M., Lam, M., Abel, G., Sotirelis, T., Greenwald, R., & Lester, M. (2005). A statistical comparison of SuperDARN spectral width boundaries and DMSP particle precipitation boundaries in the afternoon sector ionosphere. *Annales Geophysicae*, *23*(12), 3645–3654. https://doi.org/10.5194/angeo-23-3645-2005

Chisham, G., Freeman, M. P., Sotirelis, T., & Greenwald, R. A. (2005). The accuracy of using the spectral width boundary measured in off-meridional SuperDARN HF radar beams as a proxy for the open-closed field line boundary. *Annales Geophysicae*, *23*(7), 2599–2604. https://doi.org/10.5194/angeo-23-2599-2005

Chisham, G., Lester, M., Milan, S., Freeman, M., Bristow, W., Grocott, A., et al. (2007). A decade of the super dual auroral radar network (SuperDARN): Scientific achievements, new techniques and future directions. *Surveys in Geophysics*, *28*(1), 33–109. https://doi.org/10.1007/s10712-007-9017-8

Chisham, G., & Pinnock, M. (2002). Assessing the contamination of SuperDARN global convection maps by non-F-region backscatter. *Annales Geophysicae*, *20*(1), 13–28. https://doi.org/10.5194/angeo-20-13-2002

Chisham, G., Pinnock, M., & Rodger, A. S. (2001). The response of the HF radar spectral width boundary to a switch in the IMF by direction: Ionospheric consequences of transient dayside reconnection? *Journal of Geophysical Research*, *106*(A1), 191–202. https://doi.org/10.1029/2000ja900094

Cowley, S., & Lockwood, M. (1992). Excitation and decay of solar wind-driven flows in the magnetosphere-ionosphere system. *Annales Geophysicae*, *10*, 103–115.

Cowley, S., & Owen, C. (1989). A simple illustrative model of open flux tube motion over the dayside magnetopause. *Planetary and Space Science*, *37*(11), 1461–1475. https://doi.org/10.1016/0032-0633(89)90116-5

Crooker, N. (1979). Dayside merging and cusp geometry. *Journal of Geophysical Research*, *84*(A3), 951–959. https://doi.org/10.1029/ja084ia03p00951

Doss, C., Komar, C., Cassak, P., Wilder, F., Eriksson, S., & Drake, J. (2015). Asymmetric magnetic reconnection with a flow shear and applications to the magnetopause. *Journal of Geophysical Research: Space Physics*, *120*(9), 7748–7763. https://doi.org/10.1002/2015ja021489

Dungey, J. W. (1961). Interplanetary magnetic field and the auroral zones. *Physical Review Letters*, *6*(2), 47–48. https://doi.org/10.1103/physrevlett.6.47

Dunlop, M., Zhang, Q.-H., Bogdanova, Y., Trattner, K., Pu, Z., Hasegawa, H., et al. (2011). Magnetopause reconnection across wide local time. *Annales Geophysicae*, *29*(9), 1683–1697. https://doi.org/10.5194/angeo-29-1683-2011

Fear, R., Milan, S., Fazakerley, A., Lucek, E., Cowley, S., & Dandouras, I. (2008). The azimuthal extent of three flux transfer events. *Annales Geophysicae*, *26*(8), 2353–2369. https://doi.org/10.5194/angeo-26-2353-2008

Fear, R. C., Trenchi, L., Coxon, J., & Milan, S. E. (2017). How much flux does a flux transfer event transfer? *Journal of Geophysical Research: Space Physics*, *122*(12), 12–310. https://doi.org/10.1002/2017ja024730

Forsythe, V. V., & Makarevich, R. A. (2017). Global view of the e region irregularity and convection velocities in the high-latitude Southern Hemisphere. *Journal of Geophysical Research: Space Physics*, *122*(2), 2467–2483. https://doi.org/10.1002/2016ja023711

Frey, H., Phan, T., Fuselier, S., & Mende, S. (2003). Continuous magnetic reconnection at Earth's magnetopause. *Nature*, *426*(6966), 533–537. https://doi.org/10.1038/nature02084

Fuselier, S., Frey, H., Trattner, K., Mende, S., & Burch, J. (2002). Cusp aurora dependence on interplanetary magnetic field B_z. *Journal of Geophysical Research*, *107*(A7), SIA6-1–SIA6-10. https://doi.org/10.1029/2001ja900165

Fuselier, S., Petrinec, S., Trattner, K. J., Broll, J., Burch, J., Giles, B., et al. (2018). Observational evidence of large-scale multiple reconnection at the Earth's dayside magnetopause. *Journal of Geophysical Research: Space Physics*, *123*(10), 8407–8421. https://doi.org/10.1029/2018ja025681

Fuselier, S., Trattner, K., & Petrinec, S. (2011). Antiparallel and component reconnection at the dayside magnetopause. *Journal of Geophysical Research*, *116*(A10), A10227. https://doi.org/10.1029/2011ja016888

Fuselier, S., Vines, S., Burch, J., Petrinec, S., Trattner, K., Cassak, P., et al. (2017). Large-scale characteristics of reconnection diffusion regions and associated magnetopause crossings observed by MMS. *Journal of Geophysical Research: Space Physics*, *122*(5), 5466–5486. https://doi.org/10.1002/2017ja024024

Gonzalez, W., & Mozer, F. (1974). A quantitative model for the potential resulting from reconnection with an arbitrary interplanetary magnetic field. *Journal of Geophysical Research*, *79*(28), 4186–4194. https://doi.org/10.1029/ja079i028p04186

Greenwald, R. (1995). SuperDARN data [Dataset]. https://superdarn.ca

Greenwald, R., Baker, K., Dudeney, J., Pinnock, M., Jones, T., Thomas, E., et al. (1995). DARN/SuperDARN: A global view of the dynamics of high-latitude convection. *Space Science Reviews*, *71*(1–4), 761–796. https://doi.org/10.1007/bf00751350

Grimes, E. W., Harter, B., Hatzigeorgiu, N., Drozdov, A., Lewis, J. W., Angelopoulos, V., et al. (2022). The space physics environment data analysis system in python. *Frontiers in Astronomy and Space Sciences*, *9*, 1020815. https://doi.org/10.3389/fspas.2022.1020815

Hasegawa, H., Kitamura, N., Saito, Y., Nagai, T., Shinohara, I., Yokota, S., et al. (2016). Decay of mesoscale flux transfer events during quasi-continuous spatially extended reconnection at the magnetopause. *Geophysical Research Letters*, *43*(10), 4755–4762. https://doi.org/10.1002/2016gl069225

Hasegawa, H., Wang, J., Dunlop, M., Pu, Z., Zhang, Q.-H., Lavraud, B., et al. (2010). Evidence for a flux transfer event generated by multiple X-line reconnection at the magnetopause. *Geophysical Research Letters*, *37*(16), L16101. https://doi.org/10.1029/2010gl044219

Heelis, R. (1984). The effects of interplanetary magnetic field orientation on dayside high-latitude ionospheric convection. *Journal of Geophysical Research*, *89*(A5), 2873–2880. https://doi.org/10.1029/ja089ia05p02873

Hietala, H., Phan, T. D., Angelopoulos, V., Oieroset, M., Archer, M. O., Karlsson, T., & Plaschke, F. (2018). In situ observations of a magnetosheath high-speed jet triggering magnetopause reconnection. *Geophysical Research Letters*, *45*(4), 1732–1740. https://doi.org/10.1002/2017gl076525

Holzworth, R., & Meng, C.-I. (1975). Mathematical representation of the auroral oval. *Geophysical Research Letters*, *2*(9), 377–380. https://doi.org/10.1029/gl002i009p00377

Hoshi, Y., Hasegawa, H., Kitamura, N., Saito, Y., & Angelopoulos, V. (2018). Seasonal and solar wind control of the reconnection line location on the Earth's dayside magnetopause. *Journal of Geophysical Research: Space Physics*, *123*(9), 7498–7512. https://doi.org/10.1029/2018ja025305

Hudson, P. (1970). Discontinuities in an anisotropic plasma and their identification in the solar wind. *Planetary and Space Science*, *18*(11), 1611–1622. https://doi.org/10.1016/0032-0633(70)90036-x

Hunter, J. D. (2007). Matplotlib: A 2D graphics environment. *Computing in Science & Engineering*, *9*(03), 90–95. https://doi.org/10.1109/mcse.2007.55

Jain, N., Büchner, J., Dorfman, S., Ji, H., & Surjalal Sharma, A. (2013). Current disruption and its spreading in collisionless magnetic reconnection. *Physics of Plasmas*, *20*(11). https://doi.org/10.1063/1.4827828

Khanal, K. (2024). Datasets for: Controlling factors of the local time extent of magnetopause reconnection: A statistical study [Dataset]. *Zenodo*. https://zenodo.org/records/13336854

Komar, C., Fermo, R., & Cassak, P. (2015). Comparative analysis of dayside magnetic reconnection models in global magnetosphere simulations. *Journal of Geophysical Research: Space Physics*, *120*(1), 276–294. https://doi.org/10.1002/2014ja020587

Koustov, A. V., & Fiori, R. A. (2016). Seasonal and solar cycle variations in the ionospheric convection reversal boundary location inferred from monthly SuperDARN data sets. *Annales Geophysicae*, *34*(2), 227–239. https://doi.org/10.5194/angeo-34-227-2016

LaMoury, A. T., Hietala, H., Plaschke, F., Vuorinen, L., & Eastwood, J. P. (2021). Solar wind control of magnetosheath jet formation and propagation to the magnetopause. *Journal of Geophysical Research: Space Physics*, *126*(9), e2021JA029592. https://doi.org/10.1029/2021ja029592

Lockwood, M. (1997). Relationship of dayside auroral precipitations to the open-closed separatrix and the pattern of convective flow. *Journal of Geophysical Research*, *102*(A8), 17475–17487. https://doi.org/10.1029/97ja01100

Lockwood, M., Cowley, S., Sandholt, P., & Lepping, R. (1990). The ionospheric signatures of flux transfer events and solar wind dynamic pressure changes. *Journal of Geophysical Research*, *95*(A10), 17113–17135. https://doi.org/10.1029/ja095ia10p17113

Luhmann, J., Walker, R., Russell, C., Crooker, N., Spreiter, J., & Stahara, S. (1984). Patterns of potential magnetic field merging sites on the dayside magnetopause. *Journal of Geophysical Research*, *89*(A3), 1739–1742. https://doi.org/10.1029/ja089ia03p01739

McFadden, J., Carlson, C., Larson, D., Bonnell, J., Mozer, F., Angelopoulos, V., et al. (2008). Structure of plasmaspheric plumes and their participation in magnetopause reconnection: First results from THEMIS. *Geophysical Research Letters*, *35*(17), L17S10. https://doi.org/10.1029/2008gl033677

McFadden, J., Carlson, C., Larson, D., Ludlam, M., Abiad, R., Elliott, B., et al. (2008). The THEMIS ESA plasma instrument and in-flight calibration. *Space Science Reviews*, *141*, 277–302. https://doi.org/10.1007/978-0-387-89820-9_13

Meng, C.-I., Holzworth, R., & Akasofu, S.-I. (1977). Auroral circle—Delineating the poleward boundary of the quiet auroral belt. *Journal of Geophysical Research*, *82*(1), 164–172. https://doi.org/10.1029/ja082i001p00164

Milan, S., Lester, M., Cowley, S., & Brittnacher, M. (2000). Convection and auroral response to a southward turning of the IMF: Polar UVI, cutlass, and image signatures of transient magnetic flux transfer at the magnetopause. *Journal of Geophysical Research*, *105*(A7), 15741–15755. https://doi.org/10.1029/2000ja900022

Milan, S. E., Imber, S. M., Carter, J. A., Walach, M.-T., & Hubert, B. (2016). What controls the local time extent of flux transfer events? *Journal of Geophysical Research: Space Physics*, *121*(2), 1391–1401. https://doi.org/10.1002/2015ja022012

Mitchell, H., & Kan, J. (1978). Merging of magnetic fields with field-aligned plasma flow components. *Journal of Plasma Physics*, *20*(1), 31–45. https://doi.org/10.1017/s0022377800021346

Moen, J., Carlson, H., Milan, S. E., Shumilov, N., Lybekk, B., Sandholt, P., & Lester, M. (2001). On the collocation between dayside auroral activity and coherent HF radar backscatter. *Annales Geophysicae*, *18*(12), 1531–1549. https://doi.org/10.1007/s005850000302

Newell, P., Ruohoniemi, J., & Meng, C.-I. (2004). Maps of precipitation by source region, binned by IMF, with inertial convection streamlines. *Journal of Geophysical Research*, *109*(A10), A10206. https://doi.org/10.1029/2004ja010499

Ng, J., Chen, L.-J., & Omelchenko, Y. A. (2021). Bursty magnetic reconnection at the Earth's magnetopause triggered by high-speed jets. *Physics of Plasmas*, *28*(9). https://doi.org/10.1063/5.0054394

Nishimura, Y., Goldstein, J., Martinis, C., Ma, Q., Li, W., Zhang, S., et al. (2022). Multi-scale density structures in the plasmaspheric plume during a geomagnetic storm. *Journal of Geophysical Research: Space Physics*, *127*(3), e2021JA030230. https://doi.org/10.1029/2021ja030230

Nishitani, N., Ruohoniemi, J. M., Lester, M., Baker, J. B. H., Koustov, A. V., Shepherd, S. G., et al. (2019). Review of the accomplishments of mid-latitude super dual auroral radar network (SuperDARN) HF radars. *Progress in Earth and Planetary Science*, *6*, 1–57. https://doi.org/10.1186/s40645-019-0270-5

Oksavik, K., Moen, J., & Carlson, H. (2004). High-resolution observations of the small-scale flow pattern associated with a poleward moving auroral form in the cusp. *Geophysical Research Letters*, *31*(11), L11807. https://doi.org/10.1029/2004gl019838

Papitashvili, N. E., & King, J. H. (2020). Omni 1-min data [Dataset]. *NASA Space Physics Data Facility*. https://doi.org/10.48322/45bb-8792

Paschmann, G., Papamastorakis, I., Baumjohann, W., Sckopke, N., Carlson, C., Sonnerup, B. Ö., & Lühr, H. (1986). The magnetopause for large magnetic shear: AMPTE/IRM observations. *Journal of Geophysical Research*, *91*(A10), 11099–11115. https://doi.org/10.1029/ja091ia10p11099

Paschmann, G., Sonnerup, B. Ö., Papamastorakis, I., Sckopke, N., Haerendel, G., Bame, S., et al. (1979). Plasma acceleration at the Earth's magnetopause: Evidence for reconnection. *Nature*, *282*(5736), 243–246. https://doi.org/10.1038/282243a0

Phan, T., Dunlop, M., Paschmann, G., Klecker, B., Bosqued, J., Reme, H., et al. (2004). Cluster observations of continuous reconnection at the magnetopause under steady interplanetary magnetic field conditions. *Annales Geophysicae*, *22*(7), 2355–2367. https://doi.org/10.5194/angeo-22-2355-2004

Phan, T., Hasegawa, H., Fujimoto, M., Oieroset, M., Mukai, T., Lin, R., & Paterson, W. (2006). Simultaneous geotail and wind observations of reconnection at the subsolar and tail flank magnetopause. *Geophysical Research Letters*, *33*(9), L09104. https://doi.org/10.1029/2006gl025756

Phan, T., Kistler, L., Klecker, B., Haerendel, G., Paschmann, G., Sonnerup, B. Ö., et al. (2000). Extended magnetic reconnection at the Earth's magnetopause from detection of bi-directional jets. *Nature*, *404*(6780), 848–850. https://doi.org/10.1038/35009050

Phan, T., Paschmann, G., Gosling, J., Oieroset, M., Fujimoto, M., Drake, J., & Angelopoulos, V. (2013). The dependence of magnetic reconnection on plasma β and magnetic shear: Evidence from magnetopause observations. *Geophysical Research Letters*, *40*(1), 11–16. https://doi.org/10.1029/2012gl054528

Phan, T., Shay, M., Gosling, J., Fujimoto, M., Drake, J., Paschmann, G., et al. (2013). Electron bulk heating in magnetic reconnection at Earth's magnetopause: Dependence on the inflow Alfvén speed and magnetic shear. *Geophysical Research Letters*, *40*(17), 4475–4480. https://doi.org/10.1002/grl.50917

Phan, T. D., & Paschmann, G. (1996). Low-latitude dayside magnetopause and boundary layer for high magnetic shear: 1. Structure and motion. *Journal of Geophysical Research*, *101*(A4), 7801–7815. https://doi.org/10.1029/95ja03752

Pinnock, M., Chisham, G., Coleman, I., Freeman, M., Hairston, M., & Villain, J.-P. (2003). The location and rate of dayside reconnection during an interval of southward interplanetary magnetic field. *Annales Geophysicae*, *21*(7), 1467–1482. https://doi.org/10.5194/angeo-21-1467-2003

Pinnock, M., Rodger, A., Baker, K., Lu, G., & Hairston, M. (1999). Conjugate observations of the day-side reconnection electric field: A GEM boundary layer campaign. *Annales Geophysicae*, *17*(4), 443–454. https://doi.org/10.1007/s00585-999-0443-4

Rosenqvist, L., Vaivads, A., Retinò, A., Phan, T., Opgenoorth, H., Dandouras, I., & Buchert, S. (2008). Modulated reconnection rate and energy conversion at the magnetopause under steady IMF conditions. *Geophysical Research Letters*, *35*(8), L08104. https://doi.org/10.1029/2007gl032868

Ruohoniemi, J., & Baker, K. (1998). Large-scale imaging of high-latitude convection with super dual auroral radar network HF radar observations. *Journal of Geophysical Research*, *103*(A9), 20797–20811. https://doi.org/10.1029/98ja01288

Ruohoniemi, J., Greenwald, R., Baker, K., Villain, J., & McCready, M. (1987). Drift motions of small-scale irregularities in the high-latitude F region: An experimental comparison with plasma drift motions. *Journal of Geophysical Research*, *92*(A5), 4553–4564. https://doi.org/10.1029/ja092ia05p04553

Russell, C. T., & Elphic, R. (1978). Initial ISEE magnetometer results: Magnetopause observations. *Space Science Reviews*, *22*(6), 681–715. https://doi.org/10.1007/bf00212619

Russell, C. T., & Elphic, R. (1979). ISEE observations of flux transfer events at the dayside magnetopause. *Geophysical Research Letters*, *6*(1), 33–36. https://doi.org/10.1029/gl006i001p00033

Scurry, L., Russell, C., & Gosling, J. (1994). A statistical study of accelerated flow events at the dayside magnetopause. *Journal of Geophysical Research*, *99*(A8), 14815–14829. https://doi.org/10.1029/94ja00793

Shay, M., Drake, J., Swisdak, M., Dorland, W., & Rogers, B. (2003). Inherently three dimensional magnetic reconnection: A mechanism for bursty bulk flows? *Geophysical Research Letters*, *30*(6), 1345. https://doi.org/10.1029/2002gl016267

Shepherd, L., & Cassak, P. (2012). Guide field dependence of 3-DX-line spreading during collisionless magnetic reconnection. *Journal of Geophysical Research*, *117*(A10), A10101. https://doi.org/10.1029/2012ja017867

Shi, X., Schmidt, M., Martin, C. J., Billett, D. D., Bland, E., Tholley, F. H., et al. (2022). pyDARN: A Python software for visualizing SuperDARN radar data. *Frontiers in Astronomy and Space Sciences*, *9*, 1022690. https://doi.org/10.3389/fspas.2022.1022690

Sonnerup, B. Ö., & Cahill, L., Jr. (1967). Magnetopause structure and attitude from explorer 12 observations. *Journal of Geophysical Research*, *72*(1), 171–183. https://doi.org/10.1029/jz072i001p00171

Sonnerup, B. U. (1970). Magnetic-field re-connexion in a highly conducting incompressible fluid. *Journal of Plasma Physics*, *4*(1), 161–174. https://doi.org/10.1017/s0022377800004888

Sonnerup, B. U., & Scheible, M. (1998). Minimum and maximum variance analysis. *Analysis Methods for Multi-Spacecraft Data*, *1*, 185–220.

Sotirelis, T., Ruohoniemi, J., Barnes, R., Newell, P., Greenwald, R., Skura, J., & Meng, C.-I. (2005). Comparison of SuperDARN radar boundaries with DMSP particle precipitation boundaries. *Journal of Geophysical Research*, *110*(A6), A06302. https://doi.org/10.1029/2004ja010732

Swisdak, M., Opher, M., Drake, J., & Bibi, F. A. (2010). The vector direction of the interstellar magnetic field outside the heliosphere. *The Astrophysical Journal*, *710*(2), 1769–1775. https://doi.org/10.1088/0004-637x/710/2/1769

Swisdak, M., Rogers, B., Drake, J., & Shay, M. (2003). Diamagnetic suppression of component magnetic reconnection at the magnetopause. *Journal of Geophysical Research*, *108*(A5), 1218. https://doi.org/10.1029/2002ja009726

Thomas, E. G., & Shepherd, S. G. (2018). Statistical patterns of ionospheric convection derived from mid-latitude, high-latitude, and polar SuperDARN HF radar observations. *Journal of Geophysical Research: Space Physics*, *123*(4), 3196–3216. https://doi.org/10.1002/2018ja025280

Trattner, K., Mulcock, J., Petrinec, S., & Fuselier, S. (2007). Probing the boundary between antiparallel and component reconnection during southward interplanetary magnetic field conditions. *Journal of Geophysical Research*, *112*(A8), A08210. https://doi.org/10.1029/2007ja012270

Trenchi, L., Marcucci, M. F., & Fear, R. (2015). The effect of diamagnetic drift on motion of the dayside magnetopause reconnection line. *Geophysical Research Letters*, *42*(15), 6129–6136. https://doi.org/10.1002/2015gl065213

Tsyganenko, N. (1995). Modeling the Earth's magnetospheric magnetic field confined within a realistic magnetopause. *Journal of Geophysical Research*, *100*(A4), 5599–5612. https://doi.org/10.1029/94ja03193

Tsyganenko, N. A. (1989). A magnetospheric magnetic field model with a warped tail current sheet. *Planetary and Space Science*, *37*(1), 5–20. https://doi.org/10.1016/0032-0633(89)90066-4

Vines, S., Fuselier, S., Trattner, K., Burch, J., Allen, R., Petrinec, S., et al. (2017). Magnetospheric ion evolution across the low-latitude boundary layer separatrix. *Journal of Geophysical Research: Space Physics*, *122*(10), 10–247. https://doi.org/10.1002/2017ja024061

Vuorinen, L., Hietala, H., Plaschke, F., & LaMoury, A. T. (2021). Magnetic field in magnetosheath jets: A statistical study of B_z near the magnetopause. *Journal of Geophysical Research: Space Physics*, *126*(9), e2021JA029188. https://doi.org/10.1029/2021ja029188

Walsh, B., Komar, C., & Pfau-Kempf, Y. (2017). Spacecraft measurements constraining the spatial extent of a magnetopause reconnection X line. *Geophysical Research Letters*, *44*(7), 3038–3046. https://doi.org/10.1002/2017gl073379

Walsh, B., Phan, T., Sibeck, D., & Souza, V. (2014). The plasmaspheric plume and magnetopause reconnection. *Geophysical Research Letters*, *41*(2), 223–228. https://doi.org/10.1002/2013gl058802

Walsh, B., Sibeck, D., Nishimura, Y., & Angelopoulos, V. (2013). Statistical analysis of the plasmaspheric plume at the magnetopause. *Journal of Geophysical Research: Space Physics*, *118*(8), 4844–4851. https://doi.org/10.1002/jgra.50458

Wang, J., Dunlop, M., Pu, Z., Zhou, X., Zhang, X., Wei, Y., et al. (2007). TC1 and Cluster observation of an FTE on 4 January 2005: A close conjunction. *Geophysical Research Letters*, *34*(3), L03106. https://doi.org/10.1029/2006gl028241

Zou, Y., Walsh, B. M., Chen, L.-J., Ng, J., Shi, X., Wang, C.-P., et al. (2022). Unsteady magnetopause reconnection under quasi-steady solar wind driving. *Geophysical Research Letters*, *49*(1), e2021GL096583. https://doi.org/10.1029/2021gl096583

Zou, Y., Walsh, B. M., Nishimura, Y., Angelopoulos, V., Ruohoniemi, J. M., McWilliams, K. A., & Nishitani, N. (2018). Spreading speed of magnetopause reconnection X-lines using ground-satellite coordination. *Geophysical Research Letters*, *45*(1), 80–89. https://doi.org/10.1002/2017gl075765

Zou, Y., Walsh, B. M., Nishimura, Y., Angelopoulos, V., Ruohoniemi, J. M., McWilliams, K. A., & Nishitani, N. (2019). Local time extent of magnetopause reconnection using space–ground coordination. *Annales Geophysicae*, *37*(2), 215–234. https://doi.org/10.5194/angeo-37-215-2019

Zou, Y., Walsh, B. M., Shi, X., Lyons, L., Liu, J., Angelopoulos, V., et al. (2021). Geospace plume and its impact on dayside magnetopause reconnection rate. *Journal of Geophysical Research: Space Physics*, *126*(6), e2021JA029117. https://doi.org/10.1029/2021ja029117